

5-1-2016

A Case for Chiral Contributions to Nondipole Effects in Photoionization Using Linearly Polarized Soft X-rays

Kyle Patrick Bowen
University of Nevada, Las Vegas

Follow this and additional works at: <https://digitalscholarship.unlv.edu/thesesdissertations>

 Part of the [Atomic, Molecular and Optical Physics Commons](#), and the [Quantum Physics Commons](#)

Repository Citation

Bowen, Kyle Patrick, "A Case for Chiral Contributions to Nondipole Effects in Photoionization Using Linearly Polarized Soft X-rays" (2016). *UNLV Theses, Dissertations, Professional Papers, and Capstones*. 2644.
<http://dx.doi.org/10.34917/9112037>

This Dissertation is protected by copyright and/or related rights. It has been brought to you by Digital Scholarship@UNLV with permission from the rights-holder(s). You are free to use this Dissertation in any way that is permitted by the copyright and related rights legislation that applies to your use. For other uses you need to obtain permission from the rights-holder(s) directly, unless additional rights are indicated by a Creative Commons license in the record and/or on the work itself.

This Dissertation has been accepted for inclusion in UNLV Theses, Dissertations, Professional Papers, and Capstones by an authorized administrator of Digital Scholarship@UNLV. For more information, please contact digitalscholarship@unlv.edu.

A CASE FOR CHIRAL CONTRIBUTIONS TO NONDIPOLE EFFECTS IN PHOTOIONIZATION USING
LINEARLY POLARIZED SOFT X-RAYS

By

Kyle Patrick Bowen

Bachelor of Science in Chemistry
University of Nevada, Las Vegas
2009

A dissertation submitted in partial fulfillment
of the requirements for the

Doctor of Philosophy—Chemistry

Department of Chemistry and Biochemistry
College of Sciences
The Graduate College

University of Nevada, Las Vegas
May 2016



Dissertation Approval

The Graduate College
The University of Nevada, Las Vegas

April 4, 2016

This dissertation prepared by

Kyle Bowen

entitled

A Case for Chiral Contributions to Nondipole Effects in Photoionization Using Linearly Polarized Soft X-Rays

is approved in partial fulfillment of the requirements for the degree of

Doctor of Philosophy—Chemistry
Department of Chemistry and Biochemistry

Clemens Heske, Ph.D.
Examination Committee Chair

Kathryn Hausbeck Korgan, Ph.D.
Graduate College Interim Dean

Oliver Hemmers, Ph.D.
Examination Committee Member

Balakrishnan Naduvalah, Ph.D.
Examination Committee Member

Paul Forster, Ph.D.
Examination Committee Member

Bernard Zygelman, Ph.D.
Graduate College Faculty Representative

Abstract

Modelling angular distributions of photoelectrons requires making accurate approximations of both the incoming light and the behavior of bound electrons. The experimental determination of photoelectron angular distributions is crucial to the development of accurate theoretical models governing the light-matter interaction. To date, many models have relied upon the dipole approximation, which assumes a constant electric field as the source of ionization. Despite knowing that the dipole approximation would break down as photon energy increased, the precise limit was unclear. Over the past two decades, a strong case has been made that corrections to the dipole approximation are necessary for accurately describing photoionization using soft x-rays (100 – 1000 eV). This energy region is widely studied, as it has become more readily accessible thanks to third-generation synchrotron radiation facilities.

This work provides experimental evidence for first-order corrections to the dipole approximation, known as nondipole effects, for atoms and molecules, focusing on Xe 3*d* photoionization, which showcases the role of interchannel coupling in nondipole angular distributions, N 1*s* photoionization from molecular nitrogen in an attempt to settle a dispute over molecular nondipole effects, and C 1*s* photoionization from the chiral molecule camphor, which provides the first-ever experimental determination of a theoretically predicted chiral-specific nondipole effect. All of the experiments were performed using electron time-of-flight spectroscopy at the Advanced Light Source (ALS) at Lawrence Berkeley National Laboratory (LBNL).

Acknowledgements

My graduate school experience, culminating in this dissertation, has been the most defining experience of my life thus far. Over the course of my studies, I have been fortunate enough to live in dream cities like Paris and San Francisco, as well as work at some of the best scientific venues in the world, such as the Advanced Light Source (ALS) and Synchrotron SOLEIL. All of that would not have been possible without Dennis Lindle. It was so hard losing you unexpectedly. I kept you in mind every day I was writing, especially during the times I wanted to be doing something else. You'd be happy to know that your passing has brought out the best in us. Your family has taken me in, and I am fortunate to have them. Clemens Heske wanted to honor your friendship by seeing me to the finish line, and I can't thank him enough for becoming my advisor.

I would like to thank Oliver Hemmers for his unwavering support during the hard times and his encyclopedic knowledge of our experimental setup that he was always willing to share. Also, thank you Wayne Stolte for making this bookworm into a real experimentalist. It was always a pleasure turning wrenches with you. To all of my friends and collaborators over in France: Renaud Guillemin, Maria Novella Piancastelli, Denis Céolin, and Marc Simon, thank you for welcoming me to Paris and letting me share in your scientific achievements.

I'd also like to thank James Carter and Moni Blum, the staff at the ALS, as well as David Kilcoyne for helping during the last beamtime, when most of the results for this dissertation were collected.

I would like to show my appreciation for my department, run by the amazing Mark Miyamoto and Debbie Masters, who, I believe, are capable of solving every problem put in front of them. I am fortunate to have a great committee. Thank you for agreeing to be a part of all this.

I'm incredibly lucky to have the support of many friends and family members. I'm sure you all can't wait to have me back. To my mother and grandmother, who tell me they are proud of me every time we talk, I love you very much. Thank you Raquel, Catsby, and Finnegan, I truly could not have done this without the loving home you provide.

And thank you to NSF Grant 0970125 for supporting the research and the Department of Energy Office of Science for maintaining the operation of the Advanced Light Source.

Dedication

For Dennis

“the world is but a word:

Were it all yours to give it in a breath,

How quickly were it gone!”

William Shakespeare, Timon of Athens, Act II, Scene II

Table of Contents

Abstract	iii
Acknowledgements	iv
Dedication	vi
Table of Contents	vii
List of Figures	viii
Chapter 1 – An Introduction to Photoelectron Angular Distributions	1
Chapter 2 – Experimental Design	13
Chapter 3 – Atomic Nondipole Effects in Xenon 3d Photoionization	23
Chapter 4 – Molecular Nondipole Effects in Nitrogen 1s Photoionization of N₂	39
Chapter 5 – Chiral Nondipole Effects in Carbon 1s Photoionization of Camphor	51
Chapter 6 – Conclusions	66
References	69
Curriculum Vitae	85

List of Figures

Figure 1.1 Coordinate system used in determining the angular distribution of photoelectrons.....	4
Figure 3.1. Xe 3 <i>d</i> photoelectron spectrum at $h\nu = 726.0$ eV.....	24
Figure 3.2. Xe 3 <i>d</i> cross section	25
Figure 3.3. Absolute Xe 3 <i>d</i> _{5/2} photoelectron peak areas	26
Figure 3.4. Absolute Xe 3 <i>d</i> _{3/2} photoelectron peak areas	26
Figure 3.5. Xe 3 <i>d</i> _{5/2} photoelectron peak area ratios.....	27
Figure 3.6. Xe 3 <i>d</i> _{3/2} photoelectron peak area ratios.....	28
Figure 3.7. Theoretical Ne 1 <i>s</i> $\zeta(h\nu)$ values	29
Figure 3.8. Ne 1 <i>s</i> photoelectron spectrum at $h\nu = 919.8$ eV.....	29
Figure 3.9. Absolute Ne 1 <i>s</i> photoelectron peak areas	30
Figure 3.10. Ne 1 <i>s</i> photoelectron peak area ratios	31
Figure 3.11. Time-of-flight (TOF) analyzer transmission ratios	32
Figure 3.12. Xe 3 <i>d</i> _{5/2} $\beta(h\nu)$ parameters as a function of photoelectron kinetic energy	33
Figure 3.13. Xe 3 <i>d</i> _{3/2} $\beta(h\nu)$ parameters as a function of photoelectron kinetic energy	34
Figure 3.14. Xe 3 <i>d</i> _{5/2} $\zeta(h\nu)$ parameter as a function of kinetic energy	36
Figure 3.15. Xe 3 <i>d</i> _{3/2} $\zeta(h\nu)$ parameter as a function of kinetic energy	37
Figure 4.1. N 1 <i>s</i> photoelectron spectrum of N ₂ , taken at $h\nu = 433.3$ eV.....	40
Figure 4.2. Absolute N 1 <i>s</i> photoelectron peak areas as a function of kinetic energy	41
Figure 4.3. N 1 <i>s</i> photoelectron peak area ratios	42
Figure 4.4. Theoretical Ar 2 <i>p</i> $\beta(h\nu)$	43
Figure 4.5. Theoretical Ar 2 <i>p</i> $\zeta(h\nu)$	43
Figure 4.6. Ar 2 <i>p</i> photoelectron spectrum at $h\nu = 272.1$ eV.....	44
Figure 4.7. Absolute Ar 2 <i>p</i> photoelectron peak areas.....	45

Figure 4.8. Ar 2 <i>p</i> photoelectron peak area ratios.....	46
Figure 4.9. Time-of-flight (TOF) analyzer transmission ratios	46
Figure 4.10. N 1 <i>s</i> $\beta(h\nu)$ in N ₂	48
Figure 4.11. N 1 <i>s</i> $\zeta(h\nu)$ in N ₂	50
Figure 5.1. <i>R</i> - and <i>S</i> -Camphor C 1 <i>s</i> photoelectron spectrum at $h\nu = 301.0$ eV.....	54
Figure 5.2. Camphor C 1 <i>s</i> photoelectron peak area ratios.....	55
Figure 5.3. Ar 2 <i>p</i> photoelectron spectrum at $h\nu = 258.6$ eV.....	56
Figure 5.4. Ar 2 <i>p</i> photoelectron peak area ratios.....	57
Figure 5.5. Time-of-flight (TOF) analyzer transmission ratios	58
Figure 5.6. Camphor C 1 <i>s</i> $\beta(h\nu)$	59
Figure 5.7 Camphor C 1 <i>s</i> $\varepsilon(h\nu)$	61
Figure 5.8 Plots of the angular distribution probability amplitudes corresponding to the lowest kinetic energy photoelectrons studied (6.5 eV) in both <i>R</i> - and <i>S</i> -Camphor.....	62
Figure 5.9. Plots of $\beta(h\nu)$ for C 1 <i>s</i> photoionization of both enantiomers of camphor assuming no chiral nondipole effects.	63
Figure 5.10. Carbon Monoxide C 1 <i>s</i> $\varepsilon(h\nu)$	64

Chapter 1 – An Introduction to Photoelectron Angular Distributions

The study of the light-matter interaction is crucial for understanding nature from atoms to galaxies. It was Einstein's explanation of the photoelectric effect¹ that introduced the concept of light quantization, which subsequently revolutionized physics through the development of quantum mechanics, and was rewarded with a Nobel Prize. Since then, atoms have been probed with light across the electromagnetic spectrum, with these studies serving as both an inspiration and test for the development of accurate models of atomic structure and dynamics.

The basic premise of the photoelectric effect is light of a certain minimum energy will eject electrons from an atom or molecule. The minimum energy required for this process is the binding energy of the electron. Excess energy from the photon can contribute to the kinetic energy of the ejected electrons, or photoelectrons. The photon energy $h\nu$, electron binding energy $E_{binding}$, and photoelectron kinetic energy $E_{kinetic}$ are related according to:

$$h\nu = E_{binding} + E_{kinetic} \quad 1.1$$

After photoionization, the atom or molecule is left in an excited state, at which time it may relax via several processes. The two most common relaxation processes are Auger decay and radiative emission. In Auger decay, a bound electron from a higher-energy orbital fills the vacancy. In order to obey energy conservation, a third electron is ejected. The kinetic energy of the emitted electron is equal to the energy of the transition to fill the vacancy minus the

binding energy of the ejected electron. In radiative emission, once again a bound electron from a higher-energy orbital fills the vacancy left by the ejected electron, but now a photon is emitted corresponding to the energy difference. This process also obeys the conservation of energy. The ejection of an electron may also contribute to exciting an electron in a higher-energy orbital. This excited electron may remain bound or enter the continuum. These are known as shake-up and shake-off processes, respectively, and the photoelectrons with energies different from the main line are known as satellites.

This work seeks to provide experimental validation for theories describing the interaction of atoms (and molecules) with soft x-rays, a region of the electromagnetic spectrum encompassing energies between $\sim 100 - 1000$ eV. This energy region, despite becoming more readily accessible due to the advent of synchrotron radiation light sources, lacks consistent treatment in modelling the light-matter interaction. The goal of this work is to provide the justifications for the basic assumptions that must be included in any study conducted within the soft x-ray region.

The focus of this work will be on the angular distribution probabilities of electrons. As a result of direct photoionization. As will be demonstrated, angular distributions are sensitive to assumptions made about the light absorbed as well as the electronic environment of the atom or molecule. This chapter will provide highlights of the derivation of the formalism that should be used in describing the angular distribution of electrons following soft x-ray photoionization.

The probability that an electron will be ejected is given by the cross section, $\sigma(h\nu)$. The total cross section is a summation of the cross sections for individual photoionization channels,

referred to as partial cross sections. The probability that an electron will be ejected at a given angle is given by the differential cross section. Differential cross sections are more sensitive to features such as phase shifts than either total or partial cross sections. Differential cross sections are described according to:

$$\frac{d\sigma(h\nu)}{d\Omega} = \frac{1}{k} |\langle \psi_f | e^{i\mathbf{k}\cdot\mathbf{r}} \boldsymbol{\epsilon} \cdot \mathbf{p} | \psi_i \rangle|^2, \quad 1.1$$

where $d\Omega$ is a given solid angle and the squared quantity in brackets is the transition matrix elements that describe the transition from an initial state ψ_i to a final state ψ_f by a photon propagating along \mathbf{k} and with polarization $\boldsymbol{\epsilon}$. The outgoing electron is described by the position vector \mathbf{r} and the momentum vector \mathbf{p} . The term $e^{i\mathbf{k}\cdot\mathbf{r}}$ represents the spatial variation of the electromagnetic field as experienced by the absorbing charge distribution. It is here that different levels approximation can be used to simplify the differential cross section. Expanding $e^{i\mathbf{k}\cdot\mathbf{r}}$ as a Taylor series allows for a multipole interpretation of the absorbed photon. The first term in the expansion, $e^{i\mathbf{k}\cdot\mathbf{r}} = 1$, incorporates only the electric dipole (E1) component of the electromagnetic field, and is physically understood as the charge distribution experiencing a constant electromagnetic field. This approximation is referred to as the dipole approximation. The dipole approximation is valid provided the wavelength of the incoming light is much greater than the orbital occupied by the electron, $\mathbf{k} \cdot \mathbf{r} \ll 1$. Within the dipole approximation,

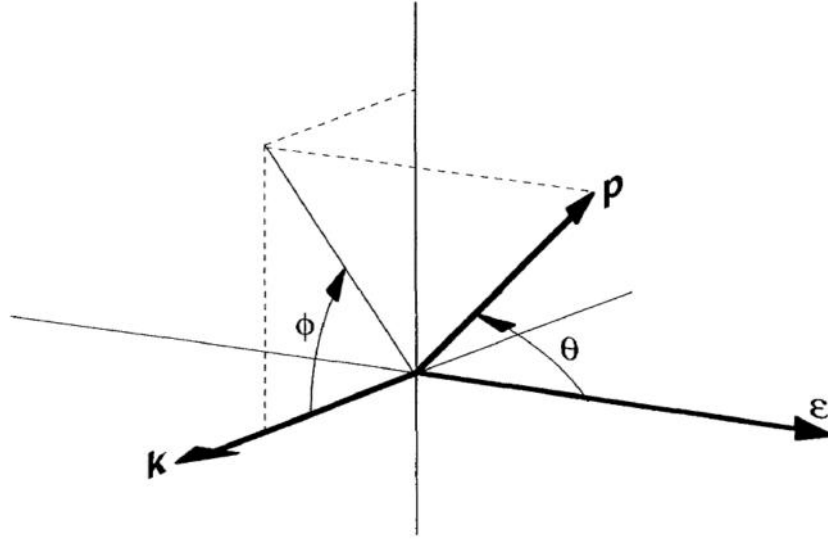


Figure 1.1 Coordinate system used in determining the angular distribution of photoelectrons. The photon beam is linearly polarized along the vector ϵ and propagating along k . The ejected electron has momentum p . Figure courtesy of Krässig²³.

the incoming photon transfers one unit of angular momentum ($l = 1$) to the electron upon absorption. This gives rise to the familiar dipole selection rules, which state that the final orbital angular momentum states possible for an electron after absorption are $l = \pm 1$.

In order to measure angular distributions within the dipole approximation, it is necessary to first define a coordinate system. The coordinate system traditionally used in describing photoelectron angular distributions is given in Figure 1.1.

Next, the differential cross section will need to be presented in terms of the coordinate system given in Figure 1.1. According to Yang², the differential cross section can be modelled by:

$$\frac{d\sigma(h\nu)}{d\Omega} = \frac{\sigma_{\text{C}}(h\nu)}{4\pi} \sum_n B_n P_n(\cos\theta), \quad 1.2$$

where ϑ is measured with respect to unpolarized photon propagation, P_n is the Legendre polynomial of order n , and B_n is a coefficient which takes into account radial matrix elements and phase shifts. A key finding of *Yang*², now referred to as Yang's Theorem, states that if transitions are induced only by waves with orbital angular momentum l , then the angular distribution of ejected particles will be given by an even polynomial of $\cos\vartheta$ with a maximum exponent of $2l$. For an electric dipole transition, $l = 1$, resulting in:

$$\frac{d\sigma(h\nu)}{d\Omega} = \frac{\sigma(h\nu)}{4\pi} [B_0 P_0(\cos\vartheta) + B_2 P_2(\cos\vartheta)]. \quad 1.3$$

For polarized light, $\cos\vartheta$ is replaced by $\cos\theta$, where θ is defined in Figure 1.1. This is due to setting $e^{ik \cdot r} = 1$ in Equation 1.1, which results in the transition operator $\epsilon \cdot \mathbf{p}$, which depends only on θ . The B_n parameters are normalized to $B_0 = 1$, and B_2 is, according to *Cooper and Zare*⁶, the angular distribution parameter, renamed $\beta(h\nu)$. This results in the following expression for the differential cross section assuming randomly oriented molecules and 100% linearly polarized light:

$$\frac{d\sigma(h\nu)}{d\Omega} = \frac{\sigma(h\nu)}{4\pi} [1 + \beta(h\nu) P_2(\cos\theta)]. \quad 1.4$$

The angular distribution parameter $\beta(h\nu)$ is related to the dipole radial matrix elements and phase shifts according to:

$$\beta(h\nu) = \frac{l(l+1)}{3} \frac{1}{\sigma_{l+1}^2 + 1} + \frac{(l+1)(l+2)}{3} \frac{1}{\sigma_{l+2}^2 + 1} - \frac{6l}{(l+1)} \frac{1}{\sigma_{l+1}^2 + 1} \cos(\delta_{l+1} - \delta_{l-1}) \quad 1.5$$

where l is a given orbital momentum state, δ_l is the phase shift of the l th partial wave, and $\sigma_{l\pm 1}$ is the dipole radial matrix element, given by:

$$\sigma_{l\pm 1}^2 = \int_0^\infty R^{nl} r R^{kl\pm 1} dr \quad 1.6$$

with R representing the radial wave functions. While the expression for $\beta(h\nu)$ developed above assumed closed-shell systems, the same expression may be used for open-shell systems²⁸.

In order to ensure physically meaningful values for the differential cross section, the dipole angular distribution parameter is limited by $-1 \leq \beta(h\nu) \leq 2$. At the lower limit, $\frac{d\sigma(h\nu)}{d\Omega} \sim \sin^2 \theta$ and electrons have maximum probability of being ejected perpendicular to both the photon propagation axis and light polarization axis and have zero probability of being ejected along the polarization axis of the incoming light. At the upper limit, $\frac{d\sigma(h\nu)}{d\Omega} \sim \cos^2 \theta$, resulting in maximum probability of photoelectrons being ejected along the polarization axis and zero probability of photoelectrons ejected vertically perpendicular to the polarization axis. It is worth noting that this value is indicative of the photoelectron as a p -wave, and is often observed for s -shell photoionization far above threshold, following dipole selection rules. The photoelectron angular distributions change gradually between the limits, with $\beta(h\nu) = 0$

representing an outgoing s -wave, and therefore an isotropic distribution. A $\beta(h\nu) = -1$ indicates that electron-electron correlations, rather than the incoming electric field, are the dominant process influencing the angular distribution²⁷.

It is possible to generalize trends in $\beta(h\nu)$ due to its dependence on orbital angular momentum, dipole radial matrix elements, and phase shifts. This work will focus on how interchannel coupling and shape resonances influence $\beta(h\nu)$. Interchannel coupling is the linear combination of all possible final state wave functions, resulting in the observable final state⁴⁴. The scale at which the individual final states contribute is directly related to their dipole transition amplitudes (cross sections), such that final states with larger cross sections will dominate the observable final state wave function. Shape resonances are resonant-like enhancements of dipole cross sections in which an outgoing electron is trapped in a metastable state. This is due to the shape of the potential acting on an outgoing electron with a particular angular momentum. Potentials that give rise to a shape resonance feature a double well. The barrier between the wells arises from the interaction between Coulombic screening and centrifugal forces³⁸. For this reason, the barriers are known as centrifugal barriers. The energy at which the shape resonance is found is determined by the penetration of the final-state wavefunction through the barrier, which increases its overlap with the initial-state wavefunction. Below this energy, the cross section is low due to suppressed electron localization probability in the barrier. The increased overlap between initial and final state wavefunctions as energy increases results in a “delayed onset” maximum in the cross section, similar to a resonance. Shape resonances are typically found near threshold. The width of the barrier is determined by the eventual dominance of the electrostatic potential, which decays as

r^{-1} , with r representing the distance from the nucleus, over the centrifugal terms, which decay as r^{-2} . This translates to short lifetimes ($\sim 10^{-17}$ s) for shape resonances, indicating that shape resonances will appear as broad features (5 – 10 eV) in the energy-dependent cross section. Furthermore, shape resonances are possible in both atoms and molecules, provided the potential meets the criteria discussed above. In atoms, it has been found that only states with orbital angular momenta $l \geq 2$ for certain atoms have the double-well potential necessary¹⁰⁹.

As photon energy increases, the wavelength of the incoming light approaches the size of the charge distribution within the atom or molecule. At this point, it becomes necessary to amend the dipole approximation. The first-order correction to the dipole approximation (often referred to as nondipole effects) incorporates the second term in the Taylor series expansion of the incoming light, $e^{i\mathbf{k}\cdot\mathbf{r}} = 1 + i\mathbf{k}\cdot\mathbf{r}$, resulting in an additional term, $(i\mathbf{k}\cdot\mathbf{r})\boldsymbol{\epsilon}\cdot\mathbf{p}$, in the transition operator. This additional term has two main consequences: it introduces cross terms featuring higher multipole interactions, namely electric dipole-electric quadrupole (E1-E2) and electric dipole-magnetic dipole (E1-M1) interactions, as well as introduces an angular dependence with respect to the photon propagation vector \mathbf{k} , which is the angle ϕ given in Figure 1.1. In following with the logic of Equation 1.2, the next term in the Taylor series expansion gives rise to inclusion of the associated B_1 and B_3 terms in the summation for the differential cross section. The B_1 and B_3 terms were parameterized similar to $\beta(h\nu)$ by Cooper²¹, and along with the incorporation of the angle ϕ , the differential cross section for 100% linearly polarized light and randomly oriented atoms or molecules becomes:

$$\frac{d\sigma(h\nu)}{d\Omega} = \frac{\sigma(h\nu)}{4\pi} \left[1 + \beta(h\nu)F^2(\cos\theta) + [\delta(h\nu) + \gamma(h\nu)\cos^2\theta] \sin^2\theta \cos^2\phi \right] \quad 1.7$$

The two new parameters, $\delta(h\nu)$ and $\gamma(h\nu)$, are referred to as the nondipole angular distribution parameters. The nondipole angular distribution parameters are dependent on orbital angular momentum and dipole and quadrupole matrix elements, along with their phase shifts. However, quadrupole matrix elements, which describe transitions obeying the selection rule $l = \pm 2$, are the dominant factor at lower energies. For this reason, large effects on dipole matrix elements may result in the enhancement of nondipole effects. Summations over the magnetic quantum number $m = 0, \pm 1$ contribute to $\gamma(h\nu)$, while only $m = \pm 1$ contribute to $\delta(h\nu)$. It is for this reason that $\delta(h\nu)$ is sometimes referred to as the “magnetic nondipole parameter” and for s subshells in the nonrelativistic case $\delta(h\nu) = 0$.

The main contribution of $\delta(h\nu)$ and $\gamma(h\nu)$ is the introduction of a forward-backward asymmetry with respect to the photon propagation direction in photoelectron angular distributions, due to the $\cos \phi$ term. Positive values for $\delta(h\nu)$ and $\gamma(h\nu)$ result in more electrons ejected in the forward direction, and for $\delta(h\nu) + \gamma(h\nu) \cos^2 \theta < 0$ more electrons are ejected in the backward direction. Values for $\delta(h\nu)$ and $\gamma(h\nu)$ are restricted to the condition $\frac{d\sigma(h\nu)}{d\Omega} \geq 0$, and therefore also depend upon $\beta(h\nu)$ values.

It has been suggested by *Grum-Grzhimailo*⁵⁰ that chiral molecules possess a unique nondipole effect. As a starting point, *Grum-Grzhimailo*⁵⁰ cites the conclusions of *Ritchie*¹³ that molecules with low enough symmetry have potentials that vary enough along the azimuthal angle ϕ as to cause inequivalent wave functions for positive and negative azimuthal quantum numbers, m . Chiral molecules lack both an inversion center and mirror symmetry, and

therefore are of sufficiently low symmetry. Within the dipole approximation, which was the formalism adopted by *Ritchie*¹³, this allowed for a nonzero B_1 term in Equation 1.2. This chiral effect within the dipole approximation is responsible for the circular dichroism seen in the angular distribution of photoelectrons, which is covered in more detail in Chapter 5. Then, analogous to the development of Equation 1.7, chiral nondipole effects should be seen in the B_2 term of Equation 1.2. When brought into agreement with the parameterization of *Cooper*²¹, the differential cross section, assuming the same conditions as Equations 1.4 and 1.7, becomes:

$$\frac{d\sigma(h\nu)}{d\Omega} = \frac{\sigma_C(h\nu)}{4\pi} [1 + \beta(h\nu) P_2(\cos\theta) + [\delta(h\nu) + \gamma(h\nu) \cos^2\theta] \sin^2\theta \cos\phi + \varepsilon(h\nu) \sin 2\theta \sin\phi], \quad 1.8$$

with the new parameter $\varepsilon(h\nu)$ termed the chiral nondipole angular distribution parameter, and $\sin 2\theta$ stemming from the trigonometric identity $\sin 2\theta = 2 \sin\theta \cos\theta$. For all achiral molecules $\varepsilon(h\nu) = 0$.

The additional term, being a nondipole term, produces an asymmetry in photoelectron angular distributions. However, for chiral molecules, the asymmetry is left-right with respect to photon propagation direction, along the photon polarization. Because the chiral molecule induced asymmetry occurs in a separate plane from achiral nondipole effects, it is possible to measure their individual contributions. However, careful experimental considerations will have to be made to measure $\beta(h\nu)$ and $\varepsilon(h\nu)$ separately (see Chapter 5). Also, it is important to distinguish between chiral nondipole effects and second-order corrections to the dipole approximation. Second-order effects incorporate the pure electric quadrupole (E2-E2) terms, as

well as interference terms between electric dipole and electric octupole (E1-E3), electric dipole and magnetic quadrupole (E1-M2), and electric quadrupole and magnetic dipole (E2-M1)⁵⁷. These interactions introduce effects in the angular distributions that overlap with $\beta(h\nu)$ contributions, and measurements often cannot distinguish between the two. However, only one experiment to date has demonstrated the role of second-order effects in photoelectron distributions⁴¹, and the conclusions from that work suggest that second-order effects are negligible until hundreds of eV above the ionization threshold. This work focuses exclusively on photoionization within 100 eV above an ionization threshold, and therefore possible second-order effects will be neglected.

There have been no experimental measurements to confirm the existence of a chiral-specific nondipole effect using linearly polarized light. This work features the first-ever measurements of the chiral nondipole parameter $\varepsilon(h\nu)$ for camphor and discusses the implications of these findings in Chapter 5. Chapters 3 and 4 give experimental evidence for the existence of nondipole effects in photoelectron angular distributions for atomic (Xe 3*d*, Chapter 3) and molecular (N₂ core-level, Chapter 4) systems. It is expected that atoms and molecules should exhibit similar behavior considering the factors that determine angular distributions of photoelectrons are dependent upon the symmetry of the charge distribution and angular momentum transfer. Starting in late 1960s, a large body of work on photoelectron angular distributions has been collected, both experimental and theoretical, and on both atoms and molecules. In fact, both Xe and N₂ have been studied in detail, and current results are compared to previous results in the respective chapters. That being said, there does not appear to be a consensus on the magnitude of nondipole effects in soft X-ray photoionization. This

work attempts to demonstrate the imperative of including nondipole effects in all descriptions of the interaction of soft x-rays with matter.

It is crucial to have an accurate understanding of the light-matter interaction on the atomic level, especially as the focus shifts to systems of greater size and complexity. Light has traditionally been vital in the study of matter, and having the proper set of expectations going into a measurement allows for more accurate conclusions to be made. And as conclusions are collected into models, it is important to have known methods to test a model's viability. It is here that measuring photoelectron angular distributions has its greatest impact.

Chapter 2 – Experimental Design

The photoelectron angular distributions are measured in this work using angle-resolved photoelectron time-of-flight (TOF) spectroscopy. This technique allows for more sensitivity in measuring the forward-backward asymmetries with respect to photon propagation that are characteristic of first-order corrections to the dipole approximation. This chapter will describe the mechanical design of a custom-built apparatus designed for use at synchrotron radiation facilities in order to perform angle-resolved electron TOF spectroscopy, as well as details in regards to data acquisition and analysis. The apparatus has been involved in the collection of data for several publications^{37, 46, 72-80} over the past two decades.

The apparatus consists of a vacuum chamber that houses five time-of-flight analyzers previously described in *Hemmers*⁷¹. Each of the analyzers is fixed at a different set of angles (θ , ϕ , see Chapter 1) in reference to the interaction region, which is defined as the volume where atoms or molecules in the gas phase intersect the incoming photon beam. The reasons for the angular positions will be discussed later in the chapter.

A 30 mm long needle with 50 μm inner diameter injects gas in an effusive flow into the interaction region. The needle can be adjusted in and out of the photon beam, and the desired position of the needle is ~ 1 mm from the beam. This results in an interaction region that is ~ 3 mm along the photon beam, and defined by the height and width of the beam (~ 1 mm \times ~ 1 mm). Gas from pressurized bottles with regulators is let into the vacuum chamber through a manifold connected to a roughing pump. A manual leak valve allows for controlled introduction of the gas into the chamber. Typical operating pressures are $\sim 10^{-5}$ Torr, which, because a needle

is used to introduce the gas into the chamber, corresponds to the greatest particle density at the interaction region ($\sim 10^{10}$ particles/mm³). This particle density ensures minimal interactions between the atoms or molecule in the interaction region. It also provides a lower load on the $1000 \frac{L}{s}$ turbomolecular pump maintaining the vacuum within the chamber.

For camphor, which is a solid at room temperature and pressure, it was necessary to develop a heating assembly which could operate during data collection. The assembly is attached to the chamber between the gas manifold and manual leak valve assembly. This allows for the changing of samples while maintaining vacuum within the chamber. The solid sample in a test tube is housed in a stainless steel container, which attaches to the chamber and the entire assembly is wrapped in heating tape. In the case of camphor, heating to 100 °C resulted in sublimation. Once the sample is in the gas phase, it is introduced through the manual leak valve. In order to ensure the sample remains in the gas phase, the needle also had to be heated. For camphor, the needle was also heated to 100 °C. The heated needle did not demonstrate any detectable effect on the data collected. However, even with the manual leak valve completely open, the maximum chamber pressure using the heated assembly on camphor was approximately ten times lower than the typical operating pressure. This could be compensated for in data collection time.

Upon photoionization, electrons, depending on their path, may enter one of the time-of-flight analyzers located < 20 mm away through a 2.0 mm aperture. A straight line path is essential for the detection of these electrons, especially at lower kinetic energies. It has been seen that magnetic fields on the order of the earth's field (~ 0.5 Gauss) can have a noticeable

effect on photoelectron paths. The interaction is kept free of stray magnetic fields through several measures. First, a μ -metal cylinder is placed around the interaction region, held in place by the TOF nozzles. This replaced three sets of Helmholtz coils, in which adjustable current through each of the sets of coils would generate a magnetic field in opposition to the magnetic field in the interaction region along the x, y, and z-axis. With the μ -metal cylinder, there is no need for the Helmholtz coils and the TOF nozzles are now essentially fixed in position, where before TOF nozzle positions could be adjusted by several millimeters for the purpose of alignment. Also in order to keep the interaction region field-free, the TOF nozzles are made of μ -metal and are electrically grounded.

After entering the first aperture, the electrons pass through a 4.0 mm diameter aperture 4.0 mm away. It is at this point that the electrons can be subjected to a retarding or accelerating voltage. The voltages are applied by a resistor cascade and can be applied using a Keithley electrometer within the range ± 250 V, as per safety restrictions. The voltages applied act as a lens system, and help optimize detection efficiency. Photoelectrons can be retarded to 2% of their initial kinetic energy without appreciable decrease in detection efficiency⁷¹. The lens system is ~ 70 mm long, after which the electrons enter a field-free drift tube, the lining of which is μ -metal. By the end of the drift tube, the electrons have traveled ~ 437.5 mm from the interaction region.

At the end of the drift tube, the electrons are detected by two 50.0 mm diameter microchannel plates (MCPs). The MCPs are made of highly resistive material with a regular array of $10\ \mu\text{m}$ channels angled at 8° from the perpendicular. An MCP, when struck by an incoming electron, will generate an electron cascade. This current acts as the measurable

signal. For the current experiment, two plates were stacked in a Chevron arrangement, in which the angled channels are rotated 180° from each other. This allows for a larger electron cascade and therefore a larger detectable current. In order to generate the electron cascade, a voltage must be applied across the MCP (~ 3200 V). Also, the MCP must be kept under vacuum, and each TOF analyzer features an $80 \frac{L}{s}$ turbo pump in order to maintain operable pressures. A safety interlock system immediately turns off the voltage in the event the chamber pressure reaches 5.0×10^{-5} Torr. Each MCP has a minimum active detection diameter of 41.9 mm, and in order to boost detection efficiency, an accelerating voltage of 500 V is applied by a honeycomb-etched mesh with 92% transmission⁷¹. The minimum active MCP areas combined with the length of the flight path results in an angular acceptance of $\pm 2.7^\circ$ for each analyzer, which corresponds to $\frac{1}{1800}$ of the total 4π solid angle.

The signal from the MCPs is then amplified and turned into a pulse using a constant fraction discriminator (CFD) (Ortec 1-GHz Amplifier and Timing Discriminator, Model 9327). The output signal from the CFD functions as the “start” in determining the electron’s flight time. A “stop” signal, provided by the synchrotron, is a NIM output (-0.8 V) mirroring the timing pattern of the light source (discussed below). The time difference between the “start” and “stop” signals is converted to a 0 – 10 V output signal (considered a “count”) utilizing a Tennelec TC 864 200 MHz time-to-amplitude converter (TAC). The TAC output voltage is converted to a channel number between 0 – 8192 by a Canberra model 8715, 800 ns fixed dead time analog-to-digital converter (ADC) in the pulse-height analysis mode. The channel information is then stored in a multichannel analyzer (MCA) (Tennelec/Oxford model PCA-Multiport-E) which

supports up to 16,384 channels from an external ADC and is capable of storing 16,777,215 counts per channel. However, the MCA is limited to ~10,000 counts/s. The MCA is read through an IEEE-488 interface card from National Instruments in a PC. The data is displayed using a custom LabView® software program from National Instruments.

It is important to note that the path of the signal as described above is for one TOF analyzer. Since there are five TOF analyzers recording simultaneously, there must be five individual sets of electronics feeding into the PC and the custom software program.

The custom LabView® software program also records the photon flux, chamber pressure, chamber angle, and retarding voltage. The photon flux is read through the same Keithley electrometer that applies the retarding voltages which is connected to the PC through an IEEE-488 interface. The chamber angle, monitored by two gravitational sensors attached to the chamber with an operating range of $\pm 45^\circ$, as well as the chamber pressure, recorded by hot-filament ion gauges, are converted to digital signals by an EKTECH remote interface which is connected to the PC through a serial connection.

For all of the data presented in this work, the vacuum chamber was connected via a thin tube differential pumping section to beamline 8.0.1 at the Advanced Light Source (ALS) at Lawrence Berkeley National Lab (LBNL) in Berkeley, CA. Beamline 8.0.1 features a 5 cm period undulator that produces ~ 100% linearly polarized light within the 80 – 1250 eV photon energy range. Three spherical monochromator gratings provide monochromatic light across the entire photon energy range. The resolving power⁸¹ ($E/\Delta E$) is 7000. All experiments are conducted during 2-bunch operation mode, which provides an x-ray pulse every 328 ns. The time between

pulses is crucial for performing electron time-of-flight measurements, as the flight times for the setup described above can roughly be calculated⁷¹ as $t(ns) = \frac{738}{\sqrt{E(eV)}}$. During normal operation (multibunch mode), the photon flux in the beamline is between $10^{11} - 10^{15}$ photons/s. During 2-bunch operation the current in the synchrotron is 40 mA. The lower flux is compensated for in measurement efficiency.

Spectra are collected for a selected time interval at one retarding or accelerating voltage for one photon energy at a time. The spectra are plotted as counts versus channels, as per the output of the ADC described above. An individual peak in any given spectrum corresponds to electrons ejected from a single orbital, providing the photon energy is above the binding energy, and the retarding voltage does not keep the electron from making it to the detector. The peaks are often several hundred channels wide and asymmetric. This arises due to the fact that the channel scale is essentially a time scale, and kinetic energy is proportional to t^{-2} . The scale could be converted via a calibration experiment, but since, as will be shown later, all of the necessary information can be gathered without such a conversion, this step was omitted.

The goal of the experiment is to determine the number of electrons corresponding to photoionization from a certain orbital according to each TOF. In order to determine the number of electrons detected by a given TOF analyzer for photoionization from any given orbital, peak areas must be determined from the spectra. This was done utilizing a built-in procedure in IGOR Pro version 6.36 from WaveMetrics, which sums all of the counts between two manually-selected cursors placed at the end points of the peak. A constant background was subtracted from each spectrum by selecting a channel value that was deemed representative of the

background. This is often sufficient because experimental noise is spread across all 8192 channels, resulting in a low, flat background.

The peak areas allow for the determination of the angular distribution parameters described in Chapter 1 according to the placement of the TOF analyzers around the interaction region. The angles (θ, ϕ) of the TOF analyzers were chosen strategically based on how their positions simplify the differential cross section. Each TOF analyzer is designated by a number (1-5). Table 2.1 provides the individual TOF designations with their angular positions, as well as the corresponding expression for the differential cross section, according to Equation 1.7. It is important to note that the chamber is able to rotate $\pm 90^\circ$ around the photon propagation axis and the angles listed are for the chamber angle used for all measurements in this work, as well as all previous published measurements using this chamber.

TOF Number	θ	ϕ	$\frac{d\sigma(h\nu)}{d\Omega}$
1	-54.7°	90.0°	$\frac{\sigma(h\nu)}{4\pi}$
2	90.0°	35.7°	$\frac{\sigma(h\nu)}{4\pi} \left[1 - \frac{\beta(h\nu)}{2} + \delta(h\nu) \sqrt{\frac{2}{3}} \right]$
3	54.7°	0.0°	$\frac{\sigma(h\nu)}{4\pi} \left[1 + (\gamma(h\nu) + 3\delta(h\nu)) \sqrt{\frac{2}{27}} \right]$
4	180.0°	90.0°	$\frac{\sigma(h\nu)}{4\pi} \left[1 + \beta(h\nu) \right]$
5	90.0°	90.0°	$\frac{\sigma(h\nu)}{4\pi} \left[1 - \frac{\beta(h\nu)}{2} \right]$

Table 2.1 The placement of each of the five time-of-flight analyzers and their corresponding expression for the differential cross section

From Table 2.1, we see that TOFs 1, 4, and 5 are independent of nondipole effects, because they are all located at $\phi = 90.0^\circ$. For that reason, this plane is referred to as the “dipole plane”. TOF 1 is independent of any angular distribution parameters, because it is located at the “magic angle”, where $P_2(\cos\theta) = 0$. This is, of course, assuming 100% linearly polarized light. For partially polarized light, the magic angle will no longer be 54.7° , and is referred to as the “quasi-magic” angle⁵³. Nondipole measurements in this work are made with TOF 3 due to its dependence on both $\delta(h\nu)$ and $\gamma(h\nu)$. It has become standard to report the measurement of nondipole angular distribution parameters as $\zeta(h\nu)$, where $\zeta(h\nu) \equiv \gamma(h\nu) + 3\delta(h\nu)$, and is referred to as the combined nondipole parameter.

Also from Table 2.1 it is possible to see how taking ratios of electron counts between TOF analyzers would result in expressions that depended solely on the angular distribution parameters, due to the occurrence of $\frac{\sigma(h\nu)}{4\pi}$ in all of the differential cross section expressions. Ratios are also convenient because, due to the fact that the spectra were collected simultaneously, effects due to gas pressure and photon flux cancel. However, ratios of TOF detector efficiencies do not cancel, and will need to be calibrated for.

In this work, $\beta(h\nu)$ is determined according to:

$$\beta(h\nu) = \frac{\text{Area TOF4} \cdot T1}{\text{Area TOF1} \cdot T4} - 1 \quad 2.1$$

$$\beta(h\nu) = 2 - 2 \frac{\text{Area TOF5} \cdot T1}{\text{Area TOF1} \cdot T5} \quad 2.2$$

where the areas represent the photoelectron peak areas for a given TOF analyzer and $\frac{T1}{T4}$ and $\frac{T1}{T5}$ represent the TOF detector efficiency ratios, referred to as transmission ratios. Transmission ratios can be determined by performing an additional experiment in the same manner discussed above for an atomic or molecular orbital with a known $\beta(h\nu)$ for photoelectrons with the same kinetic energy. Substituting the known $\beta(h\nu)$ in Equation 2.1 or 2.2 allows for the determination of the transmission ratios.

Similarly, the combined nondipole parameter $\zeta(h\nu)$ is determined by:

$$\zeta(h\nu) = \sqrt{\frac{27}{2} \left(\frac{Area\ TOF3}{Area\ TOF1} \cdot \frac{T1}{T3} - 1 \right)}. \quad 2.3$$

A discussion of the determination of the chiral nondipole parameter from Equation 1.8 will be given in Chapter 5.

Errors in this measurement stem from uncertainties in photon wavelength, the flight length of the photoelectrons, and flight time. Based on the stated resolving power of the beamline, the uncertainty in wavelength is $\ll 1\%$. Variations in flight length stems from the size of the interaction region, but the small acceptance angle limits the uncertainty to ~ 0.5 mm over a total 437.5 mm flight path⁷¹. This uncertainty also contributes to the uncertainty in flight time, but the uncertainty in flight time changes with kinetic energy⁷¹. For photon kinetic energies up to 100 eV, energy resolution for the detectors is typically ~ 100 meV. These uncertainties depend upon ideal operation of the beamline optics. This experiment assumes

100% linear polarization, and deviations would require utilizing the polarization-dependent differential cross section expressions given by *Shaw*²⁹. As an example, 95% polarization would introduce $\sim 8\%$ error in $\beta(h\nu)$ measurements when $(h\nu) = 2$, and roughly twice as much error in $\zeta(h\nu)$. Additional error would also be introduced by any instability in the beam position. The angles of the TOF analyzers are in reference to the interaction region, which changes as the beam intersects different regions of the gas emerging from the needle.

To conclude, the experiment designed to determine angular distribution parameters has been described in detail. In essence, ratios of electron counts in select time-of-flight analyzers allows for the individual determination of the parameters $\beta(h\nu)$ and $\zeta(h\nu)$. The general methods of analysis and calibration utilized in data analysis have also been discussed.

Chapter 3 – Atomic Nondipole Effects in Xenon 3*d* Photoionization

Photoionization of the outer subshells of xenon has long been a topic of interest in atomic physics, in particular in order to understand the nuances of interchannel coupling. Interchannel coupling (see Chapter 1) has been used to explain nondipole effects seen at photon energies as low as a few tens of eV in Xe 5*s* and 5*p* photoionization^{78, 93, 94, 96}, as well as an unexpected sharp deviation from $\beta(h\nu) = 2$ for Xe 5*s* photoionization well above threshold^{78, 94, 96}. Interchannel coupling also explains the results of Xe 4*p* photoionization, as the photoionization cross section is influenced heavily by the dominant Xe 4*d* channel⁸⁵. This work presents an experimental determination of the angular distribution parameters $\beta(h\nu)$ and $\zeta(h\nu)$ for Xe 3*d* photoionization for photoelectron kinetic energies up to 75 eV above threshold. From these measurements, it is possible to deduce the role of interchannel coupling in photoionization and demonstrate the necessity of first-order corrections to the dipole approximation in the description of the light-matter interaction for atoms.

Previous work on Xe 3*d* photoionization has provided a theoretical^{52, 96, 97} and experimental^{85, 92} determination of $\beta(h\nu)$. This work provides the first experimental determination of the Xe 3*d* $\zeta(h\nu)$ parameter, which is a direct determination of the magnitude of first-order corrections to the dipole approximation (see Chapter 1). The current $\zeta(h\nu)$ measurements will be compared to previously published calculations^{91, 101}.

Xe 3*d* photoelectron spectra were collected as described in Chapter 2 within the photon energy range 681.5 – 749.0 eV. An example is shown in Fig. 3.1 (photon energy: 726.0 eV). The beamline photon energy was calibrated according to Xe absorption in the region of the Xe 3*d*_{3/2}

absorption peak, centered at 700.7 eV⁹⁷. The photoelectron kinetic energies are in reference to the tabulated Xe 3d binding energies of 676.4 eV for Xe 3d_{5/2} and 689.0 eV for Xe 3d_{3/2}¹⁰⁷. Spectra were collected for 900 seconds and retarding voltages in the range of -35 V to 15 V were applied in order to keep the photoelectrons detected by the channel plates at roughly the same kinetic energy (see Chapter 2). The gas pressure within the chamber was approximately 10⁻⁶ Torr.

The number of electrons detected in TOF analyzers 1, 3, and 4 as a result of Xe 3d_{5/2} or Xe 3d_{3/2} photoionization were determined by integrating the respective peak from the photoelectron spectrum and the data was analyzed as described in Chapter 2.

The absolute peak areas for each TOF analyzer as a function of photoelectron kinetic energy are presented in Figures 3.2 (Xe 3d_{5/2}) and 3.3 (Xe 3d_{3/2}). In principle, the behavior of the

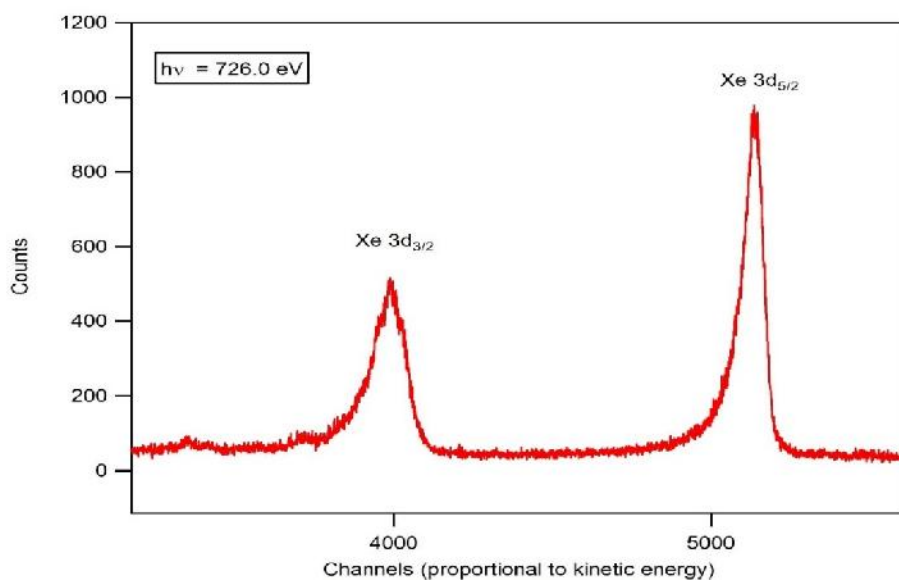


Figure 3.1. Xe 3d photoelectron spectrum at $h\nu = 726.0$ eV

peak area curves should mimic the photoionization cross section, with TOF 4 dependent also on $\beta(h\nu)$ and TOF 3 dependent on $\beta(h\nu)$ and $\zeta(h\nu)$ (see Table 2.1). The Xe 3d photoionization cross section, as shown in Figure 3.2, features two broad maxima centered around 688 and 702 eV and are attributed to 3d $\rightarrow \epsilon f$ shape resonances¹⁰³. Shape resonances are enhancements in photoionization cross sections caused by above-threshold metastable states. An outgoing electron is trapped in this metastable state until it enters the continuum via tunneling. The 3d $\rightarrow \epsilon f$ shape resonances are responsible for the two maxima in the Xe 3d_{5/2} absolute peak area plots centered at ~ 10 eV and ~ 27 eV kinetic energy for all TOF analyzers as seen in Figure 3.3. The same shape resonances are responsible for the first maximum in the Xe 3d_{3/2} absolute peak areas (see Figure 3.4) as well as the apparent shoulder at ~ 15 eV (Figure 3.4, highlighted section). There also appears to be a maxima centered at ~ 28 eV kinetic energy in all TOF analyzers for Xe 3d_{3/2} photoionization, which is not found in previous cross section calculations¹⁰².

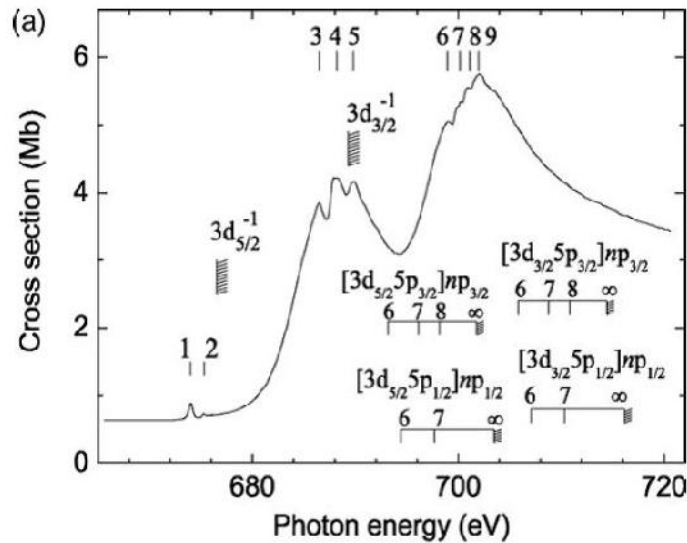


Figure 3.2 Xe 3d cross section as measured by Kato¹⁰³.

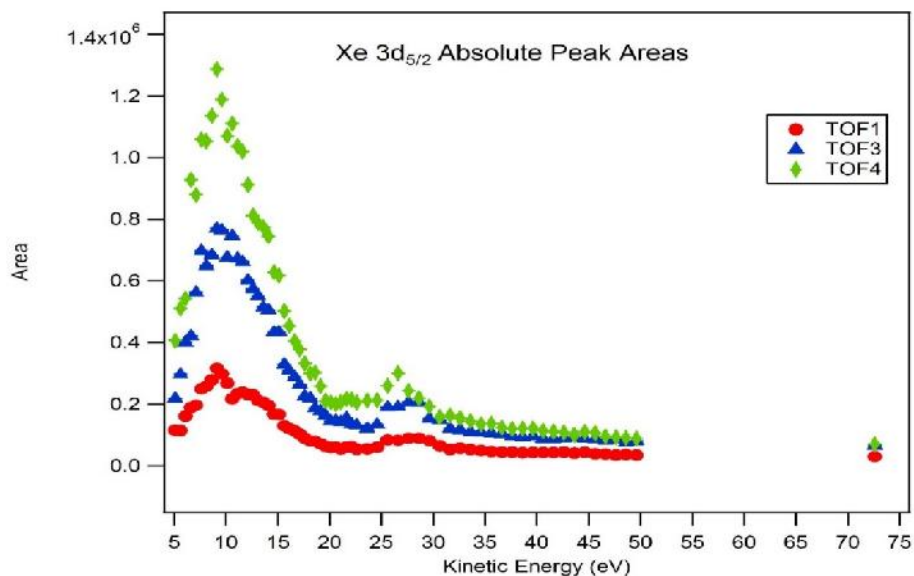


Figure 3.3. Absolute Xe $3d_{5/2}$ photoelectron peak areas. The two maxima correspond to the locations of two $3d \rightarrow \epsilon f$ shape resonances.

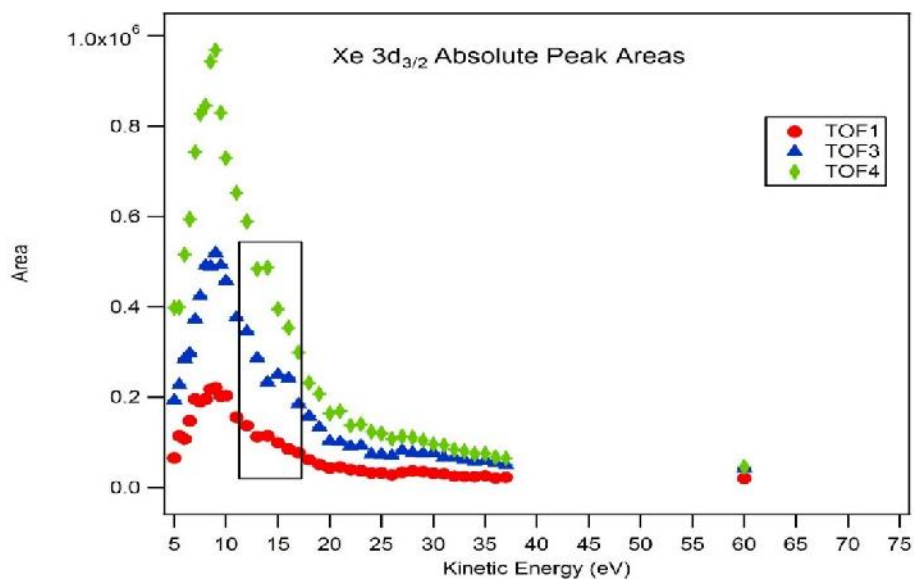


Figure 3.4. Absolute Xe $3d_{3/2}$ photoelectron peak areas. The highlighted region indicates the presence of a small shoulder at ~ 15 eV for all of the TOFs.

The angular distribution parameters $\beta(h\nu)$ and $\zeta(h\nu)$ are related to ratios of absolute peak areas between analyzers, according to Equations 2.1 and 2.3. In this particular case, TOF analyzers 4 and 1 were compared in order to determine $\beta(h\nu)$, and analyzers 3 and 1 to determine $\zeta(h\nu)$. Kinetic-energy-dependent peak-area ratios between TOF analyzers 3 and 1, as well as TOF analyzers 4 and 1 are given in Figures 3.5 (Xe $3d_{5/2}$) and 3.6 (Xe $3d_{3/2}$). We find that the peak area ratios vary as smooth curves except for the kinetic energy regions corresponding to the maxima in the absolute peak areas. We would expect, according to Equations 2.1 and 2.3, that these features in the peak area ratios, if not accounted for in the electron detector efficiency ratios (calibration measurements, see below), should correspond to maxima or minima in the $\beta(h\nu)$ and $\zeta(h\nu)$ parameters.

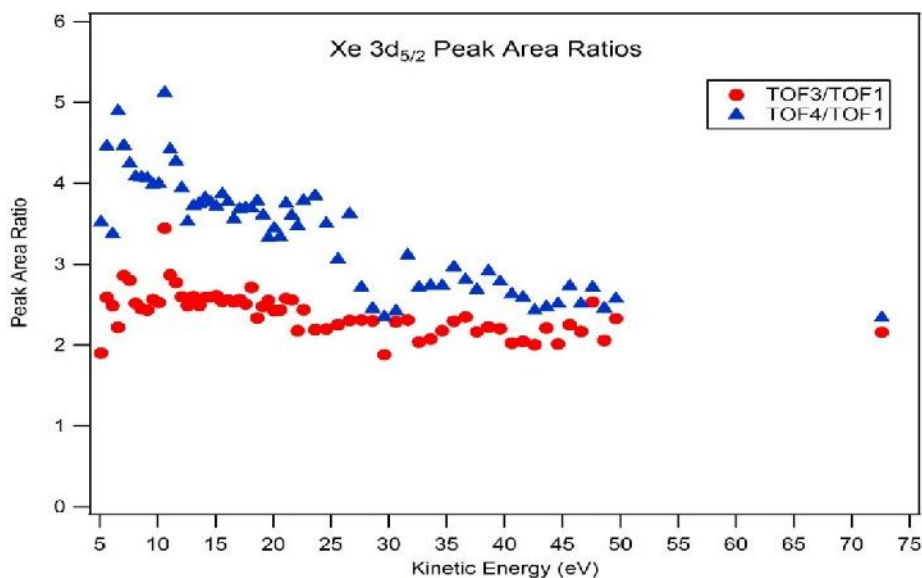


Figure 3.5. Xe $3d_{5/2}$ photoelectron peak area ratios

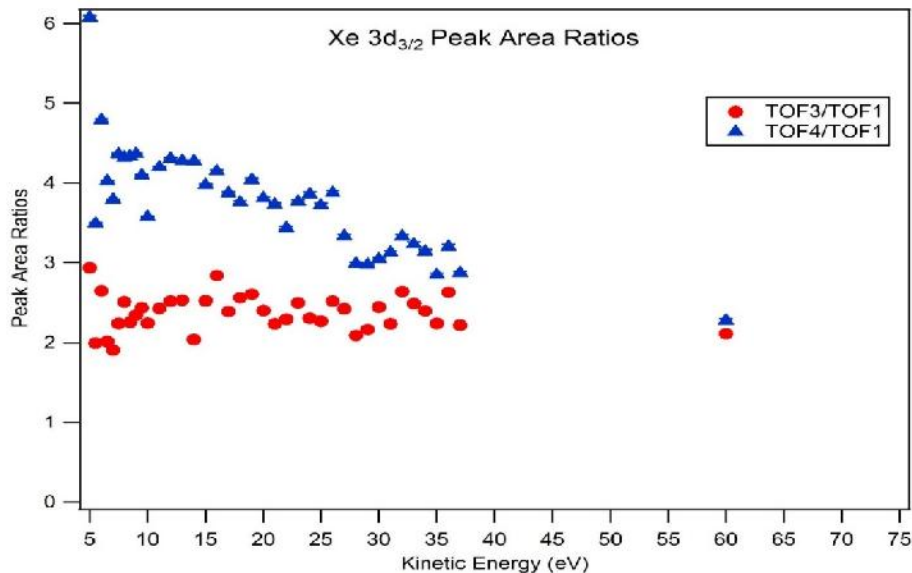


Figure 3.6. Xe 3d_{3/2} photoelectron peak area ratios

In order to calibrate the electron detector efficiencies, it is necessary to determine the transmission ratios, as described in Chapter 2. The resultant efficiency ratios appear as the $\frac{T_1}{T_4}$ and $\frac{T_1}{T_3}$ terms in Equations 2.1 and 2.3, respectively. The transmission ratios were determined by measuring Ne 1s photoionization, for which $\beta(h\nu) = 2$, and $\zeta(h\nu)$ was determined theoretically⁹¹ within the photoelectron kinetic energy range of interest, and are plotted in Figure 3.7.

Ne 1s spectra were collected within the same photoelectron kinetic energy range as the Xe 3d data shown above, in reference to the Ne 1s binding energy of 870.2 eV¹⁰⁷. A sample Ne 1s spectrum is presented in Figure 3.8 (photon energy of 919.8 eV).

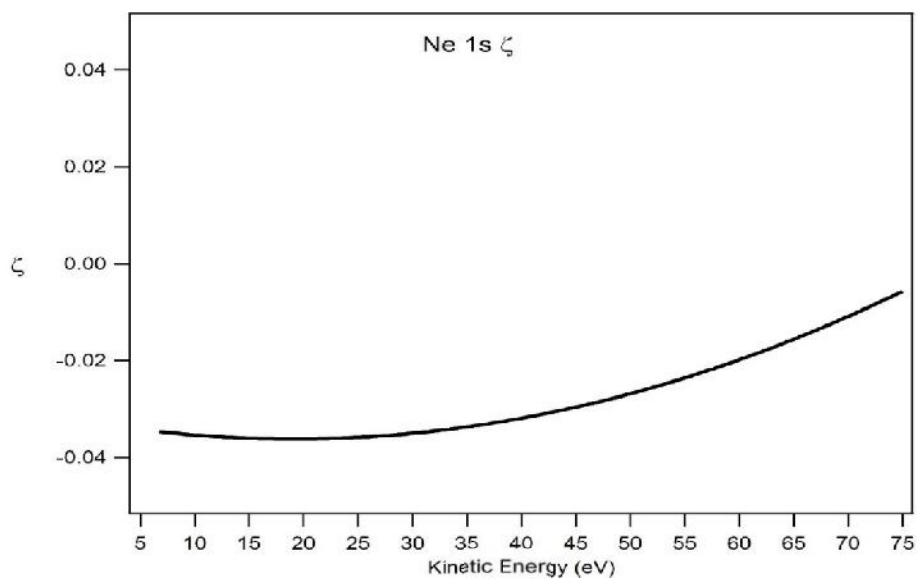


Figure 3.7. Theoretical Ne 1s $\zeta(h\nu)$ values from Derevianko⁹¹

The Ne 1s data was subjected to the same analysis procedure as the Xe 3d data.

Absolute peak areas for Ne 1s are presented in Figure 3.9.

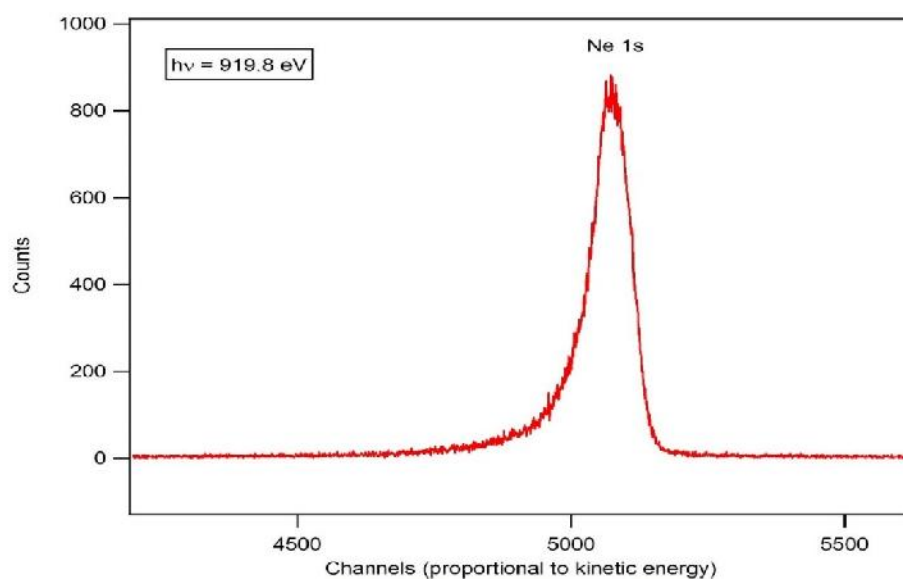


Figure 3.8. Ne 1s photoelectron spectrum at $h\nu = 919.8$ eV

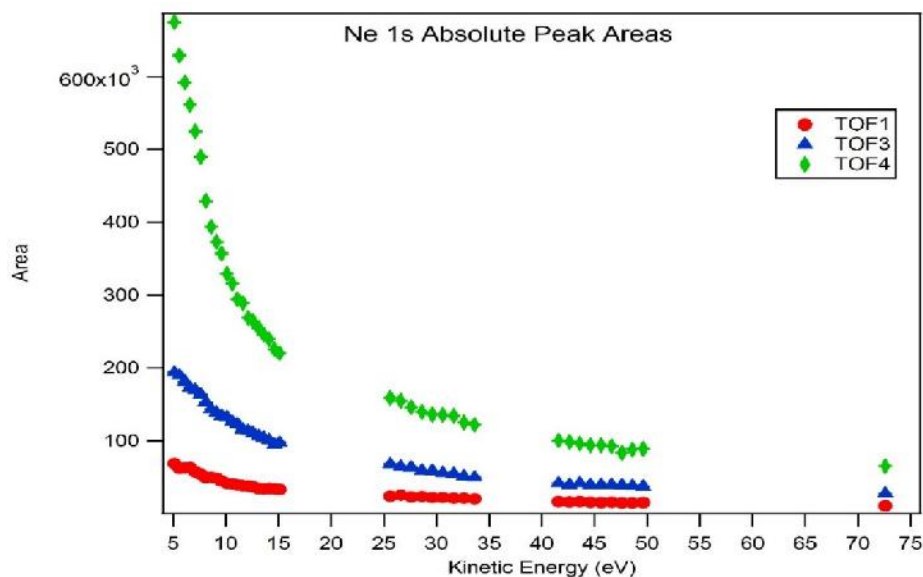


Figure 3.9. Absolute Ne 1s photoelectron peak areas

We see that the photoelectron intensity falls off smoothly as the energy increases above threshold, consistent with Ne 1s photoionization cross section calculations³⁶. The gaps in the absolute peak area plot are a result of “beam loss” during the experiment (it is not unusual that the electron beam in the storage ring of the synchrotron radiation facility is “lost” from time to time). Unfortunately, access to the photon beam ended before data for these energies could be collected. The photoionization cross section is not expected to have any features within the energy regions for which there is no data, and the missing data does not correspond to where features are seen in the Xe 3*d* measurements. The subsequent Ne 1s peak area ratios for TOF analyzers 4 and 1, as well as 3 and 1, are presented in Figure 3.10.

We see that the smoothly varying absolute peak areas correspond to smoothly varying peak area ratios in this case. This implies that the features seen in the Xe 3*d* measurements are real, and not an experimental artifact.

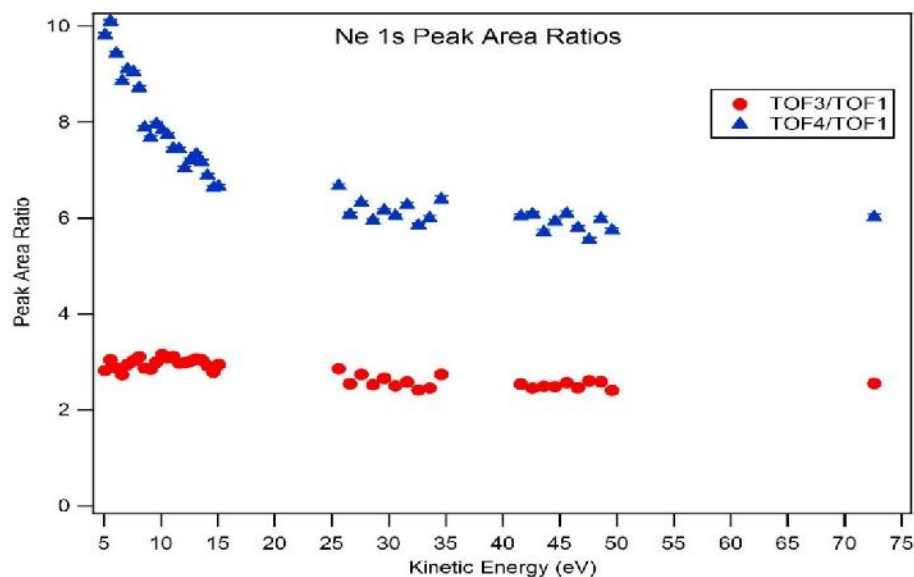


Figure 3.10. Ne 1s photoelectron peak area ratios

Transmission ratios were determined according to Equations 2.1 and 2.3. Figure 3.11 is a plot of the transmission ratios as a function of photoelectron kinetic energy. The plot was fit with a smooth curve, as the detectors described in Chapter 2 do not display any resonant absorption features, and detector efficiency tends to increase with kinetic energy for photoelectrons in the energy range of the present work. Therefore, it is expected that ratios of detector efficiencies should be smoothly varying.

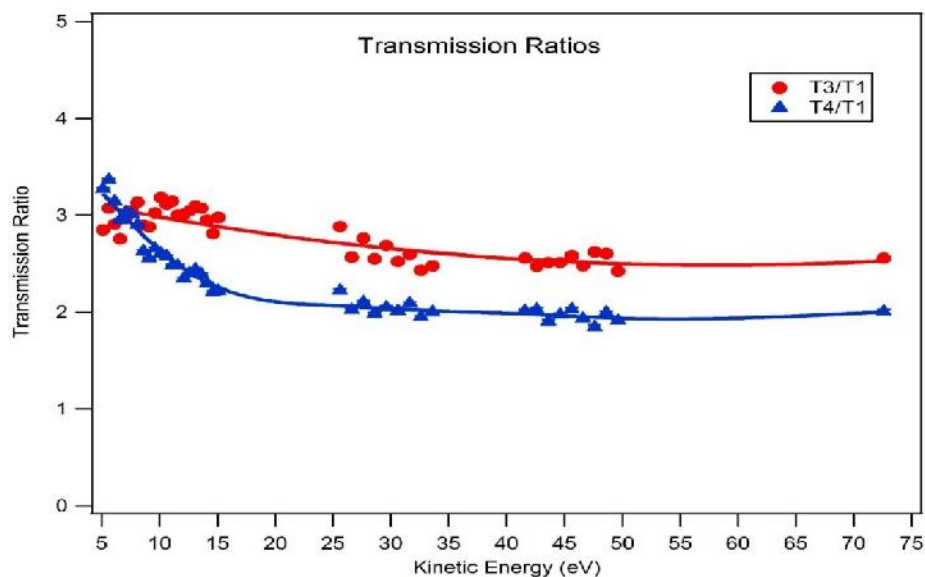


Figure 3.11. Time-of-flight (TOF) analyzer transmission ratios. The solid lines are smooth fits as described in the chapter.

The smooth fits were used to determine $\beta(h\nu)$ for Xe $3d_{5/2}$ and Xe $3d_{3/2}$ photoionization according to Equation 2.1. The results are presented in Figures 3.12 ($3d_{5/2}$) and 3.13 ($3d_{3/2}$). There are similar trends in $\beta(h\nu)$ for both Xe $3d_{5/2}$ and Xe $3d_{3/2}$ photoionization. At low photoelectron kinetic energies, $\beta(h\nu)$ is near zero but positive, and increases rapidly with increasing photoelectron kinetic energy until $\beta \sim 0.7 \pm 0.1$ above 10 eV kinetic energy. As kinetic energy increases, $\beta(h\nu)$ slowly declines, except for within the range of 25 - 35 eV kinetic energy, which features a minimum centered at ~ 30 eV. The minimum $\beta(h\nu)$ value is $\sim 0.1 \pm 0.1$ for Xe $3d_{5/2}$ and $\sim 0.4 \pm 0.1$ for Xe $3d_{3/2}$. The minima for $3d_{5/2}$ can be attributed to the shape resonance centered at 702 eV, in which the $3d \rightarrow \epsilon f$ dipole matrix elements are much smaller than the $3d \rightarrow \epsilon p$ matrix elements, resulting in a decrease in $3d_{5/2}$ ⁹⁸. However, the effect in the Xe $3d_{3/2}$ $\beta(h\nu)$ curve is attributed to the unexpected maxima seen in the current measurements.

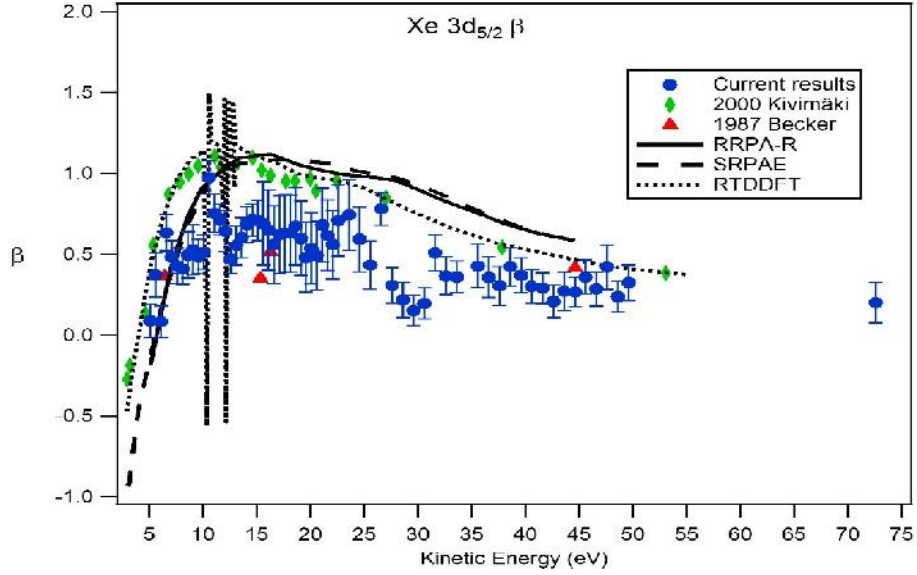


Figure 3.12. *Xe 3d_{5/2} S parameters as a function of photoelectron kinetic energy. The blue circles represent the new data presented in this work, compared to experimental results from Kivimäki⁹² (green diamonds) and Becker⁸⁵ (red triangles). The experimental values are compared with relativistic random phase approximation with relaxation (RRPA-R) calculations from Radojević⁹⁵ (solid black line), spin-polarized random phase approximation with exchange (SRPAE) calculations from Amusia⁹⁸ (dashed black line), as well as relativistic time-dependent density functional theory (RTDDFT) calculations from Toffoli⁹⁷ (dotted black line).*

Error bars for the current measurements are deduced from the difference in $\beta(h\nu)$ from assuming a point-by-point transmission ratio versus assuming the transmission ratio as a linear fit, as well as accounting for the effects of imperfect polarization and TOF positions being within $\pm 1^\circ$ of their ideal positions.

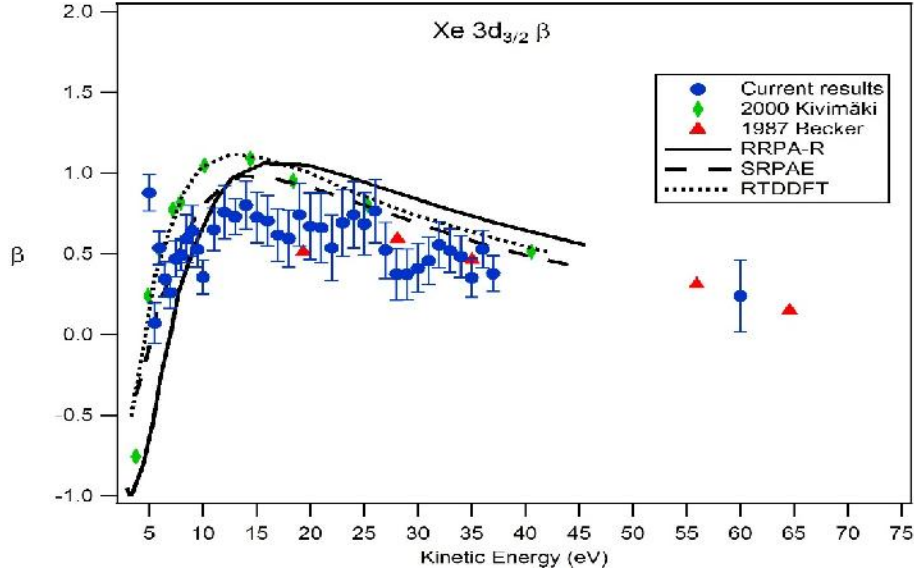


Figure 3.13. *Xe 3d_{3/2} S parameters as a function of photoelectron kinetic energy. The blue circles represent the new data presented in this work, compared to experimental results from Kivimäki⁹² (green diamonds) and Becker⁸⁵ (red triangles). The experimental values are compared with relativistic random phase approximation with relaxation (RRPA-R) calculations from Radojević⁹⁵ (solid black line), spin-polarized random phase approximation with exchange (SRPAE) calculations from Amusia⁹⁸ (dashed black line), as well as relativistic time-dependent density functional theory (RTDDFT) calculations from Toffoli⁹⁷ (dotted black line).*

The current experimental $\beta(h\nu)$ values are compared with previous electron time-of-flight measurements^{85, 92}. The current results agree well with Becker⁸⁵ (red triangles), as data was collected in a similar fashion. However, differences exist between the current results and Kivimäki⁹² (green diamonds), which we attribute to differences in experimental geometry. In Kivimäki⁹², $\beta(h\nu)$ is determined from electrons scattered in the backward direction relative to the direction of the incoming photon. This is precisely where first-order nondipole corrections effect the angular distributions of photoelectrons. The authors recognized this and yet assumed negligible nondipole effects based on calculations from Cooper²¹. However, the calculations from Cooper²¹ are not within the energy range of the data in question. No such assumptions had to be made for the current results, due to the experimental geometry (see Chapter 2).

The experimental $\beta(h\nu)$ results are also compared with relativistic random phase approximation with relaxation calculations⁹⁵, spin-polarized random phase approximation with exchange (SRPAE) calculations⁹⁸, as well as relativistic time-dependent density functional theory (RTDDFT) calculations⁹⁷. There is reasonable agreement between all the calculations, with the RTDDFT calculations demonstrating strong oscillations in Xe $3d_{5/2}$ $\beta(h\nu)$ parameter before the Xe $3d_{3/2}$ threshold, attributed to autoionizing resonances. This could account for the maximum near 10 eV kinetic energy seen in the current measurements. All calculations demonstrate a subtle feature in $\beta(h\nu)$ for Xe $3d_{5/2}$ near the $3d \rightarrow \epsilon f$ shape resonance at 702 eV (~ 28 eV photoelectron kinetic energy). The calculations are in good agreement with the measurements from *Kivimäki*⁹². However, this feature is of smaller magnitude compared to current measurements, and a maximum as opposed to a minimum. All calculations attribute this feature to interchannel coupling, as does *Kivimäki*⁹², and yet this feature is absent in Xe $3d_{3/2}$ $\beta(h\nu)$. The decrease of $3d \rightarrow \epsilon f$ dipole matrix elements across the shape resonance should result in a decrease in $\beta(h\nu)$ ⁹⁸, which is contradictory to the results. It should be noted that all theoretical calculations reference exclusively the experimental results from *Kivimäki*⁹², making no reference to *Becker*⁸⁵. It would be worthwhile to see if any amendments made to the calculations could account for the behavior as is seen in the current measurements of the Xe $3d$ $\beta(h\nu)$ parameter in the region of the $3d \rightarrow \epsilon f$ shape resonance centered at 702 eV.

In addition to $\beta(h\nu)$, the first-order combined nondipole parameter, $\zeta(h\nu)$, was determined according to Equation 2.3 and using smooth fit values for the transmission ratio. The results are presented in Figures 3.14 and 3.15 for Xe $3d_{5/2}$ and Xe $3d_{3/2}$, respectively. In Figure 3.14, the Xe $3d_{5/2}$ $\zeta(h\nu)$ is fairly constant within error across the kinetic energy range

studied, with the exception of a larger effect seen near threshold. The error bars were determined in the same manner as for $\beta(h\nu)$. For perspective, $\zeta(h\nu) = -0.5$ would correspond to $\sim 24\%$ more electrons being ejected in the backward direction relative to the incoming photon beam. For Xe $3d_{3/2}$, $\zeta(h\nu)$ is similar to the results for Xe $3d_{5/2}$ at higher kinetic energies, but shows large oscillations near threshold.

Current experimental results differ from relativistic independent particle approximation (R IPA) calculations⁹¹, as well as spin-polarized random phase approximation with exchange (SRPAE) calculations¹⁰¹, which indicate that there are no nondipole effects within this energy range. However, according to the work of *Hansen et al.*⁷², the independent particle approximation (IPA) would not be an accurate description of Xe $3d$ photoionization due to the presence of interchannel coupling. The SRPAE calculations do take interchannel coupling into effect, and yet do not show any nondipole effects.

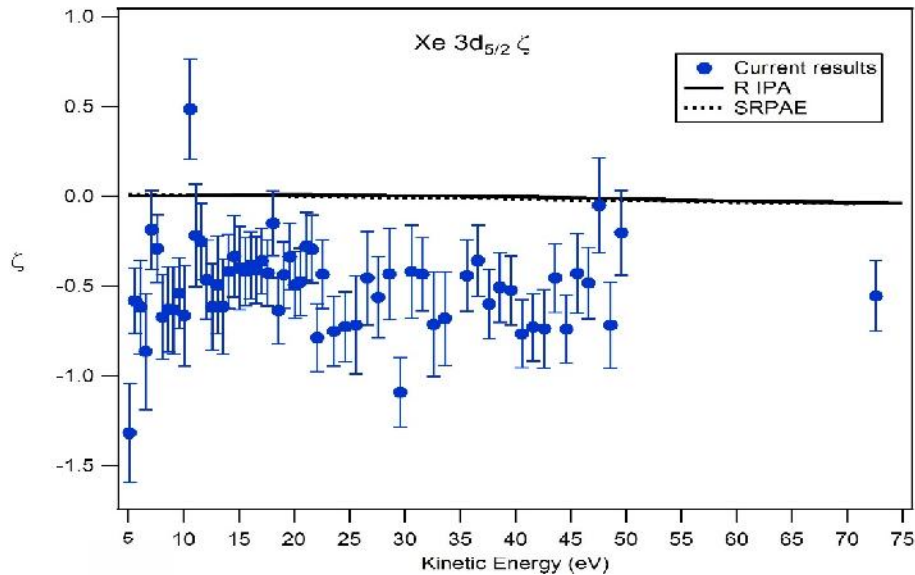


Figure 3.14. Xe $3d_{5/2}$ $\zeta(h\nu)$. The blue circles represent experimental results from this work, compared to relativistic independent particle approximation (R IPA) calculations from Dereviako⁹¹ (solid black line), as well as spin-polarized random phase approximation with exchange (SRPAE) calculations from Amusia¹⁰¹ (dotted black line).

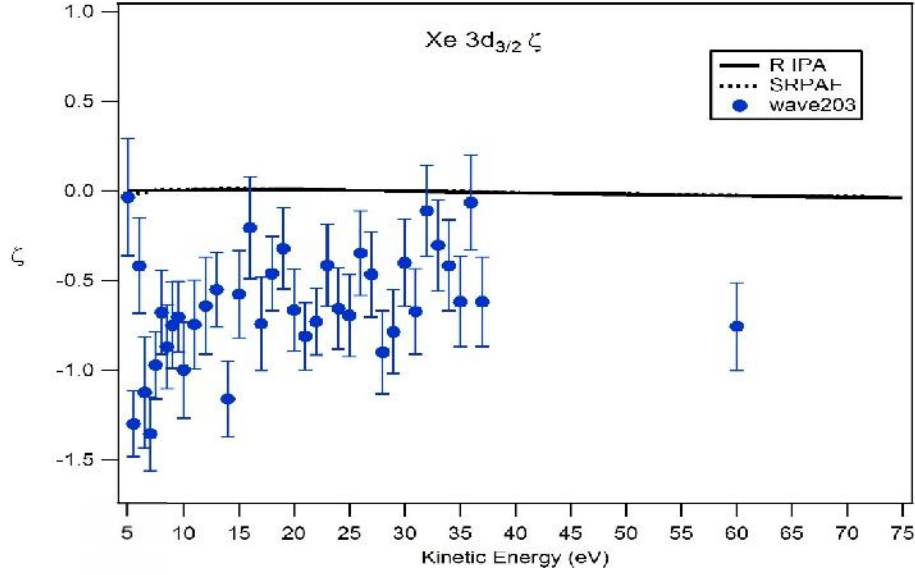


Figure 3.15. $\text{Xe } 3d_{3/2} \zeta(h\nu)$. The blue circles represent experimental results from this work, compared to relativistic independent particle approximation (R IPA) calculations from Derevianko⁹¹ (solid black line), as well as spin-polarized random phase approximation with exchange (SRPAE) calculations from Amusia¹⁰¹ (dotted black line).

In conclusion, angular distribution parameters $\beta(h\nu)$ and $\zeta(h\nu)$ were determined experimentally for Xe $3d$ photoionization near threshold. The results are compared with existing measurements and calculations. Resonant features in $\beta(h\nu)$ are measured at the corresponding location of $3d \rightarrow \epsilon f$ shape resonances, with an additional feature in the Xe $3d_{3/2}$ $\beta(h\nu)$ currently unexplained by existing theory. The relatively large effect for Xe $3d_{5/2}$ $\beta(h\nu)$ is due to coupling with the Xe $3d_{3/2}$ channel. Differences between our results and other published experimental measurements are explained by different experimental geometries. The disagreement between current $\beta(h\nu)$ results and theory is worthy of further investigation. Measurements of $\zeta(h\nu)$ from this work indicate a significant nondipole effect, with $\sim 24\%$ more electrons being ejected in the backward direction relative to the incoming photon beam. This result is absent in theoretical calculations. While this is to be expected for the calculations performed using the independent particle approximation, as they neglect interchannel

coupling, it is unclear why the SRPAE calculations, which include interchannel coupling, do not agree with the current experimental results. What is clear from the present results is that first-order corrections to the nondipole approximation are necessary for an accurate depiction of Xe $3d$ photoionization. Furthermore, Xe $3d$ is not a special case; it fits in well with the current body of work on nondipole effects in soft x-ray photoionization, and it is expected that the conclusions from the current results could be extended to photoionization in other atoms.

Chapter 4 – Molecular Nondipole Effects in Nitrogen 1s Photoionization of N₂

With the necessity of first-order nondipole effects for a complete description of soft x-ray photoionization established for atoms, it is logical to next examine molecular soft x-ray photoionization. The nitrogen molecule is an ideal candidate, as it is diatomic and homonuclear. To date, angular distributions of photoelectrons from molecular nitrogen have been investigated extensively both experimentally^{75, 77, 114, 119, 124, 126, 131} and theoretically^{73, 94, 115, 117, 129, 130}. However, the role of nondipole effects still remains in question. Original work^{75, 76, 77} suggested large, resonant nondipole effects at about 60 eV above the N 1s photoionization threshold, which were attributed to an unprecedented discovery of bond-length dependence in nondipole parameter calculations. However, subsequent works^{124, 129 - 131} did not find any measurable nondipole effects within the first hundred eV above the N 1s photoionization threshold. The current work, which utilizes an upgraded experimental setup from *Hemmers*⁷⁴, was thus undertaken to provide definitive results for the role of nondipole effects in molecular nitrogen between 20 and 90 eV above the N 1s photoionization threshold. It is also the hope that the results for N₂ will be analogous to all nondipole effects in molecules.

Molecular nitrogen N 1s electron time-of-flight spectra were collected as described in Chapter 2 in the photon energy range of 432.3 – 499.3 eV. This range begins just above the broad σ^* shape resonance, centered at 419 eV¹⁰⁹. The beamline photon energy was calibrated to the N 1s $\rightarrow 2\pi_g^*$ absorption of N₂ at 400.88 eV¹¹⁶. The pressure in the chamber was $\sim 10^{-6}$ Torr. Each spectrum was recorded for 600 seconds and retarding voltages were applied within the nozzles of the time-of-flight (TOF) analyzers to ensure that electrons with roughly the same

kinetic energy would be detected by the microchannel plates (see Chapter 2). This corresponded to a range of voltages between 2 – 70 V across the data set. Photoelectron kinetic energies are in reference to the N 1s binding energy of 409.9 eV¹¹⁰ for N₂.

A sample N 1s electron time-of-flight spectrum is presented in Figure 4.1 (photon energy of 433.3 eV). The peak is broad due to the unresolved vibrational states.

The total number of electrons collected within each TOF analyzer as a result of N 1s photoionization is represented by the area under the N 1s peak. Peak areas were further analyzed as described in Chapter 2.

A plot of the absolute N 1s peak areas for each TOF analyzer as a function of photoelectron kinetic energy is presented in Figure 4.2. The features at low kinetic energy are possibly an experimental artifact, as the energies are too high to be associated with the σ^* shape resonance. Note that the photon energy steps were reduced between 49.4 and 69.4 eV

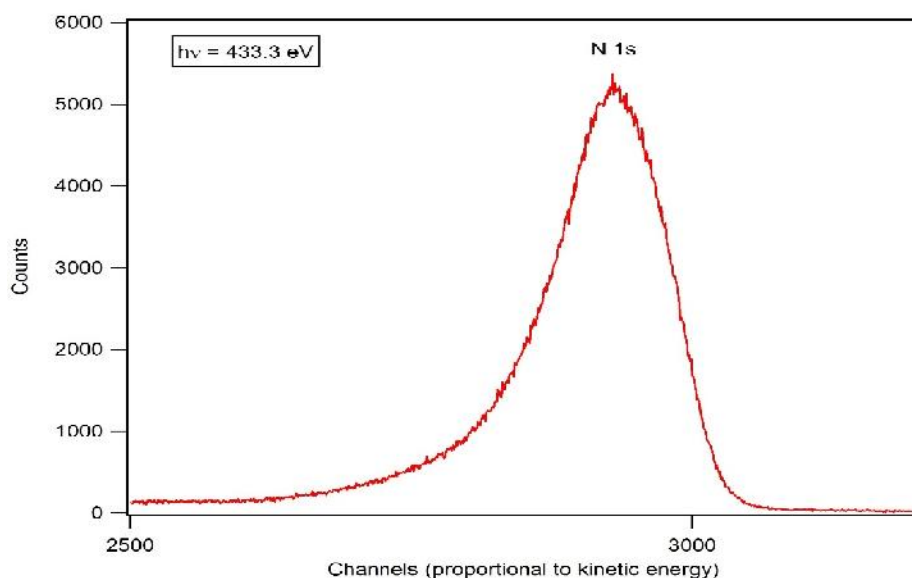


Figure 4.1. N 1s photoelectron spectrum of N₂, taken at $h\nu = 433.3$ eV

photoelectron kinetic energy in order to allow for a detailed analysis of the photon energy range in which, previously, nondipole effects were reported as most prominent⁷⁵.

Ratios of absolute peak areas allow for the determination of the angular distribution parameters $\beta(h\nu)$ and $\zeta(h\nu)$ according to Equations 2.1 - 2.3. In this work, $\beta(h\nu)$ is determined using the ratio of TOF analyzers 4 and 1, with the ratio of analyzers 5 and 1 serving as a consistency check. The $\zeta(h\nu)$ parameter is determined from the ratio of TOF analyzers 3 and 1. In Figure 4.3, these particular peak area ratios as a function of photoelectron kinetic energy are presented.

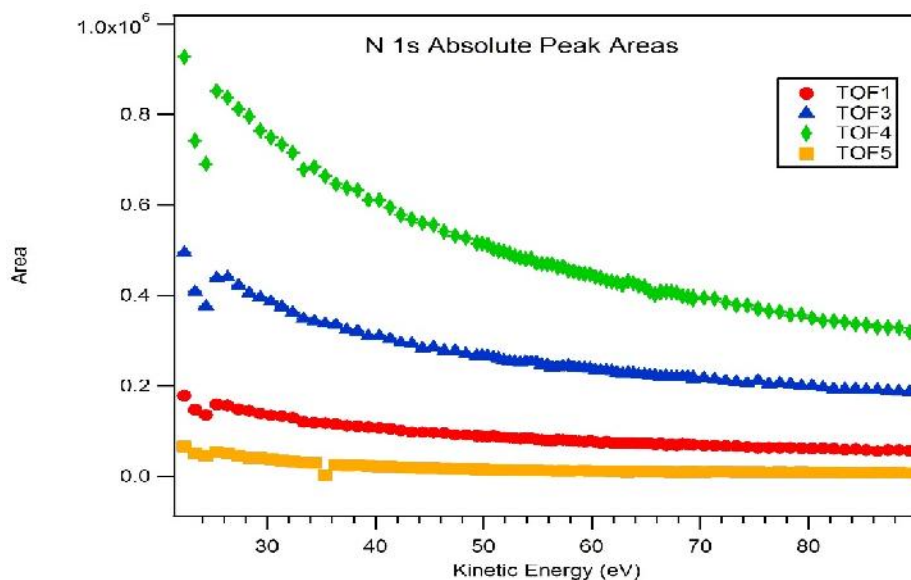


Figure 4.2. Absolute N 1s photoelectron peak areas as a function of kinetic energy

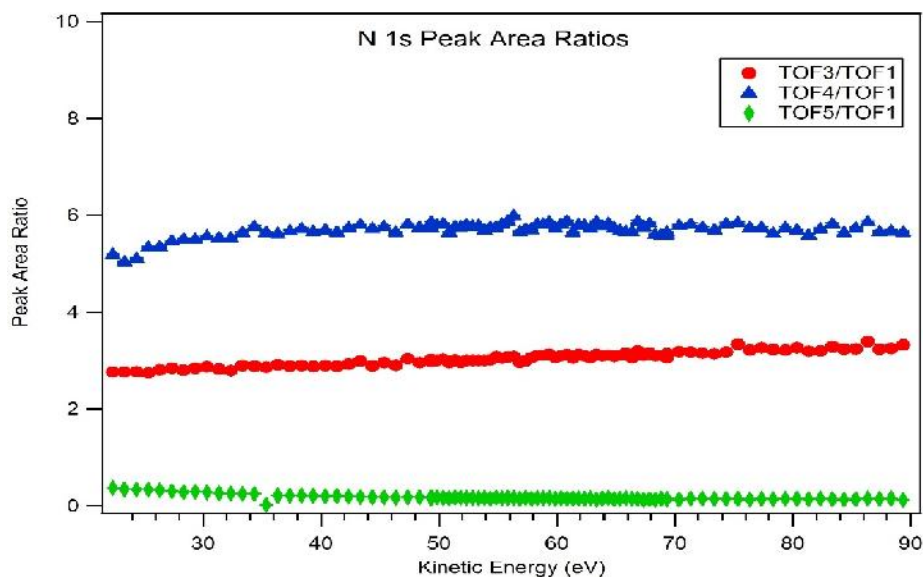


Figure 4.3. *N 1s photoelectron peak area ratios*

In order to determine $\beta(h\nu)$ and $\zeta(h\nu)$ for N_2 , the associated analyzer transmission ratios first need to be determined. For this purpose Ar 2*p* photoionization was chosen, as $\beta(h\nu)$ and $\zeta(h\nu)$ for Ar 2*p* have been calculated within the same photoelectron kinetic energy range⁹¹. The Ar 2*p* $\beta(h\nu)$ parameter as a function of photoelectron kinetic energy is presented in Figure 4.4, and $\zeta(h\nu)$ in the same energy range is given in Figure 4.5.

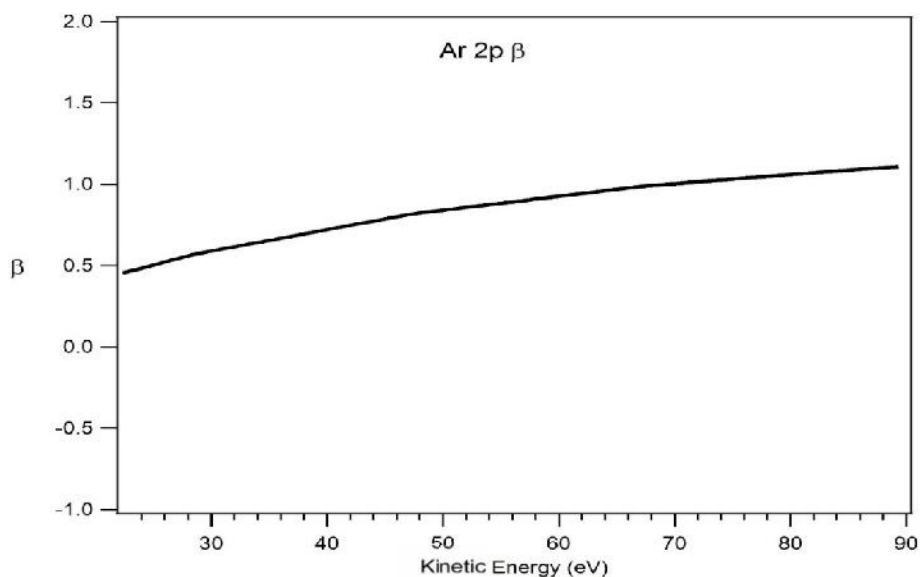


Figure 4.4. Theoretical Ar 2p $\beta(h\nu)$ parameter according to Derevianko⁹¹

Ar 2p photoelectron spectra were collected during the same experimental run as the molecular nitrogen data. Spectra were collected within the energy range 271.1 – 338.1 eV so the N 1s and Ar 2p photoelectrons had the same kinetic energy in the two experiments. Spectra

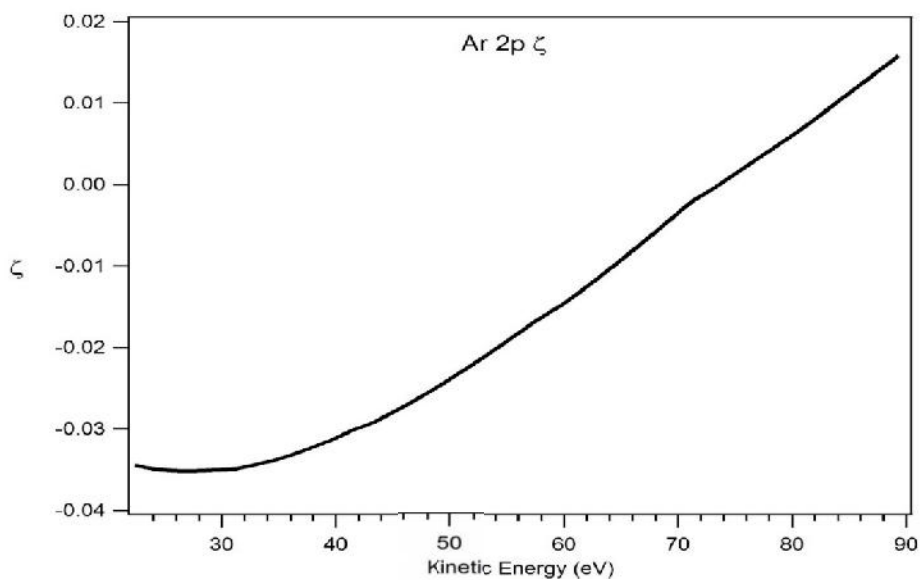


Figure 4.5. Theoretical Ar 2p $\zeta(h\nu)$ parameter according to Derevianko⁹¹

were collected for 600 seconds and with the same retarding voltages as for N₂. These measures ensure that the Ar 2p_{1/2} and Ar 2p_{3/2} photoelectron peaks span roughly the same time channels as the corresponding N 1s photoelectron peak in N₂. The beamline photon energy was calibrated in reference to Ar 2p → 4s absorption, centered at 244.4 eV¹²⁰. Ar 2p photoelectron kinetic energies are reported in reference to binding energies¹⁰⁷ of 248.4 eV for Ar 2p_{3/2} and 250.6 eV for Ar 2p_{1/2}. An Ar 2p sample spectrum at a photon energy of 272.1 eV is presented in Figure 4.6.

The Ar 2p data was analyzed using the same methods as the N₂ data (see Chapter 2). Due to the partial overlap of the two lines, the area of the entire doublet-peak was derived (rather than deriving two separate areas for Ar 2p_{1/2} and 2p_{3/2}). The thus-determined absolute peak areas for each TOF analyzer as a function of photoelectron kinetic energy are presented in

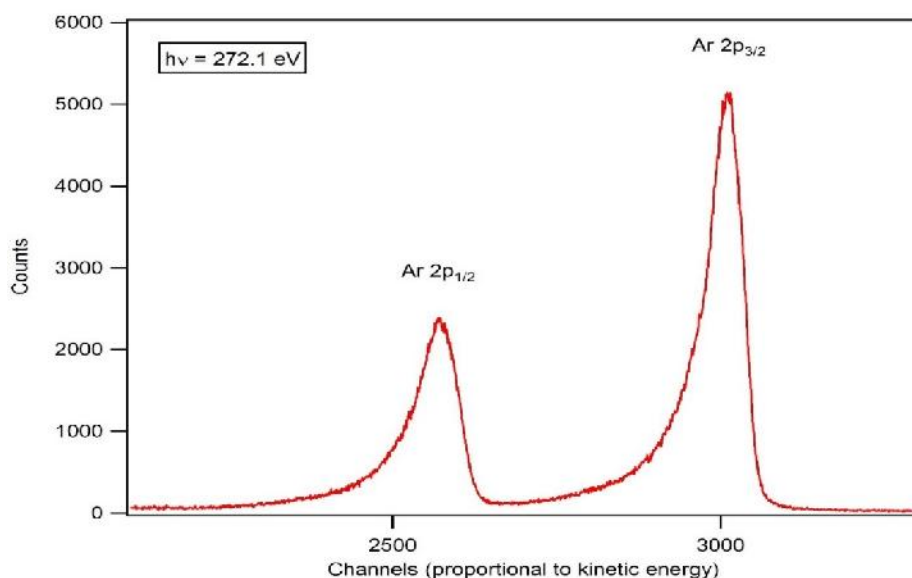


Figure 4.6. Ar 2p photoelectron spectrum at $h\nu = 272.1$ eV

Figure 4.7. The two minima present in all of the analyzers are due to decreased photon flux around the carbon K-edge, a common feature of soft x-ray beamlines. Carbon layers accumulate on the optics and absorb photons at distinct energies. However, these “carbon dips” are removed when determining peak area ratios of different analyzers for the same photon energy scan. However, the presence of carbon may result in decreased polarization due to elastic scattering. As a result, the error bars for the angular distribution parameters incorporate the effects of imperfect polarization (see below). The peak area ratios, comparing TOF analyzers 3, 4, and 5 to TOF analyzer 1 as a function of photoelectron kinetic energy, are presented in Figure 4.8.

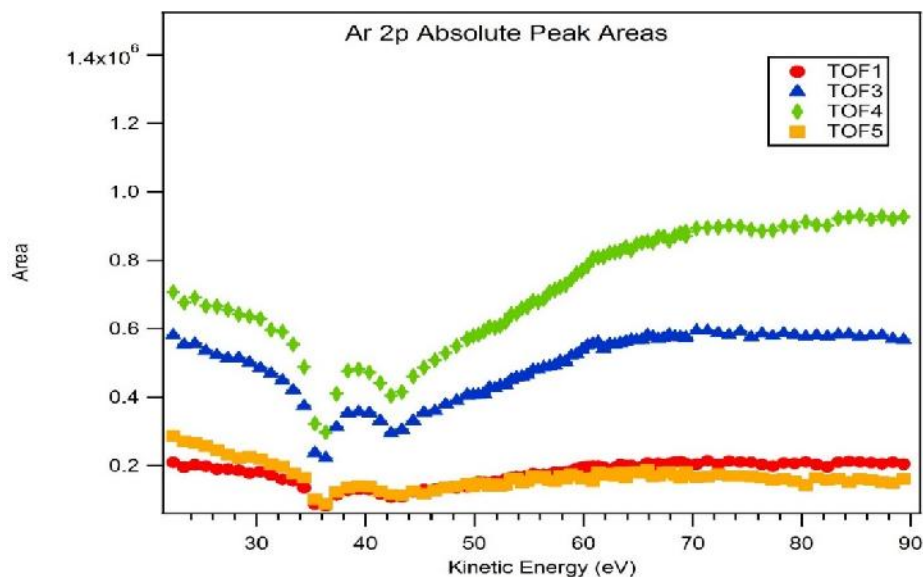


Figure 4.7. Absolute Ar 2p photoelectron peak areas

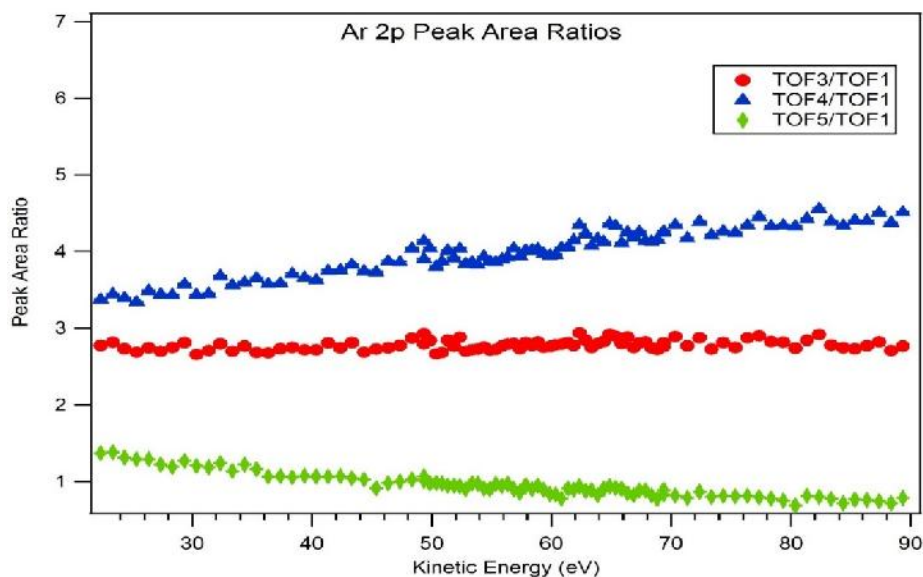


Figure 4.8. Ar 2p photoelectron peak area ratios

Transmission ratios, determined according to Equations 2.1 - 2.3, are presented in Figure 4.9. The plots have been fit with smooth curves, following the logic outlined in Chapter 3. The fit values are then used in the determination of the angular distribution parameters $\beta(h\nu)$ and $\zeta(h\nu)$.

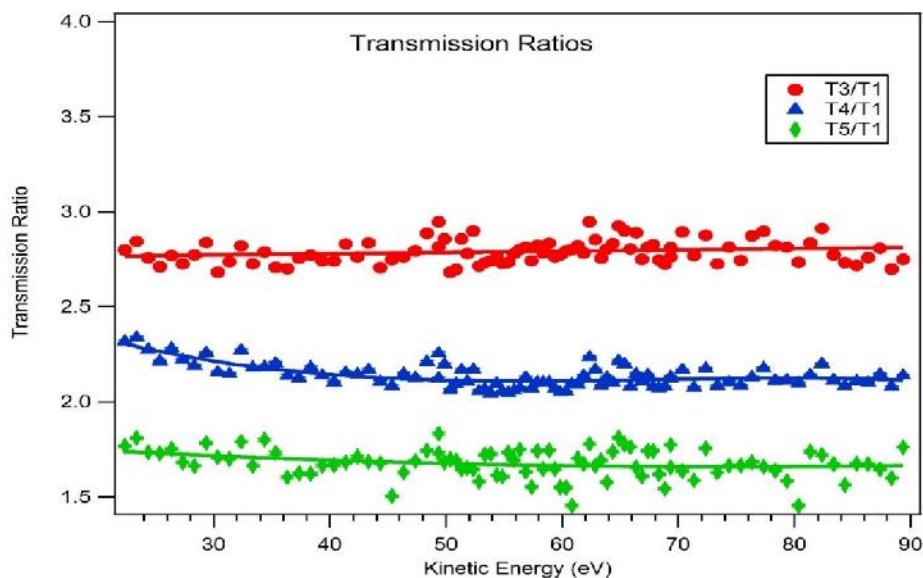


Figure 4.9. Time-of-flight (TOF) analyzer transmission ratios. The solid lines are smooth fits as described in the chapter.

$\beta(h\nu)$ for N 1s photoelectrons in N₂ within the range of 22 – 90 eV kinetic energy was determined according to averaging the results from equations 2.1 and 2.2, and is presented in Figure 4.10. We see that, for low kinetic energies, $\beta(h\nu)$ is $\sim 1.4 \pm 0.2$ and approaches $\sim 1.7 \pm 0.2$ as the kinetic energy increases to ~ 50 eV, and remains essentially constant for the remainder of the energy range presented. The error bars for the present results were determined from the difference in the TOF4/TOF1 and TOF5/TOF1 $\beta(h\nu)$ measurements, as well as incorporating any effects due to imperfect polarization and TOF angles being within $\pm 1^\circ$ of their ideal positions.

Previous measurements are plotted with the current results. These include electron time-of-flight measurements^{76, 114, 119}, and electron-ion coincidence measurements^{124, 131}, as well self-consistent X α calculations¹¹⁷, *ab initio* calculations⁷³, and density functional theory, single-center expansion (DFT-SCE) calculations¹²⁸. In general, there is good agreement between all experiments and theory, with the exception of the earliest experimental results from *Lindle*¹¹⁴ (red triangles). The current results essentially overlap the findings of *Bolognesi*¹³¹, and for that reason the points are hard to discern in the figure. The *ab initio* calculations from *Arce*⁷³ and the experimental results in *Langhoff*⁷⁶ differ from current results, and find that $\beta(h\nu) = 2$ for all kinetic energies above 50 eV. The reason for this discrepancy is unknown. The general behavior is consistent with trends in $\beta(h\nu)$ at increasing energies above the ionization threshold.

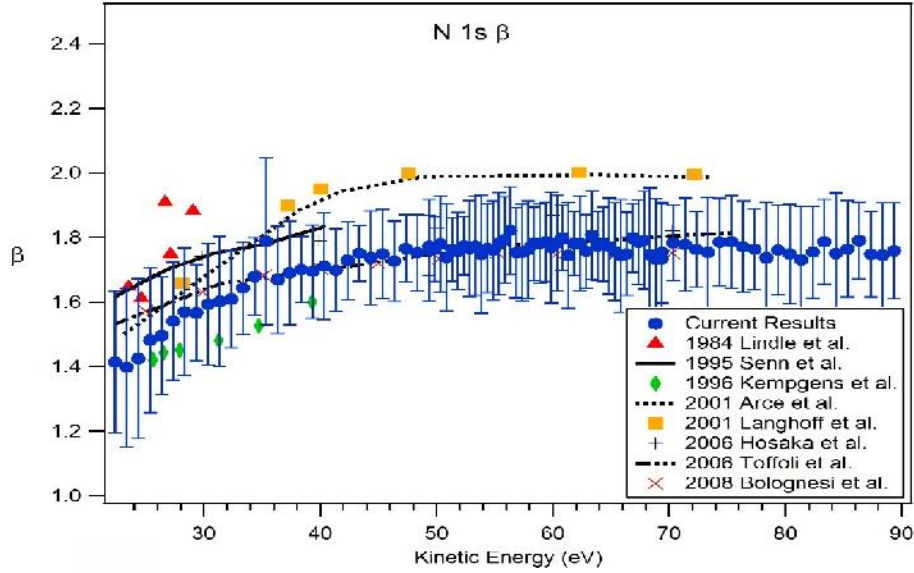


Figure 4.10. $N\ 1s\ \beta(h\nu)$ in N_2 . The blue circles represent the present results, compared to experimental results from Lindle¹¹⁴ (red triangles), Kempgens¹¹⁹ (green diamonds), Langhoff⁷⁶ (orange squares), Hosaka¹²⁴ (crosses), and Bolognesi¹³¹. Results are also compared with self-consistent $X\alpha$ calculations from Senn¹¹⁷, *ab initio* calculations from Arce⁷³ and Langhoff⁷⁶, as well as density functional theory, single-center expansion (DFT-SCE) calculations from Toffoli¹²⁹.

Figure 4.11 presents the results for the combined first-order nondipole parameter, $\zeta(h\nu)$, determined in the same manner as $\beta(h\nu)$. Values for $\zeta(h\nu)$ increase between zero and $\sim 0.5 \pm 0.4$ within the energy range studied. Error bars were determined in the same manner as for $\beta(h\nu)$.

From the plot, one can deduce three different sets of results. Original electron time-of-flight measurements⁷⁴ with corresponding *ab initio* calculations⁷⁶ conclude that there are significant nondipole effects within this energy range, with a broad maximum around 60 eV. Electron-ion coincidence, or so-called “fixed-in-space” measurements from Guillemin⁷⁷ agree with the findings of Hemmers⁷⁴ and Langhoff⁷⁶. The maximum is explained by bond-length dependent terms in the calculation of $\zeta(h\nu)$ ⁸¹. Contrary to this, electron-ion coincidence measurements performed using velocity-imaging techniques¹²⁴ and electrostatic hemispherical

analyzers¹³¹, as well as self-consistent X α and density functional theory, single-center expansion (DFT-SCE) calculations suggest there are no significant nondipole effects within the same photoelectron kinetic energy range for N 1s photoionization in N₂. In the particular case of calculations from *Bolognesi*¹³¹, it is suggested that nondipole effects are present in the photoionization from the individual $1\sigma_g$ and $1\sigma_u$ orbitals, but these effects interfere destructively, resulting in $\zeta(h\nu) = 0$. The present results indicate the emergence of nondipole effects at ~ 20 eV kinetic energy. The $\zeta(h\nu)$ parameter increases to $\sim 0.5 \pm 0.4$ within the region studied, which implies an approximate 24% asymmetry in the electrons ejected in the forward direction with respect to the incoming photon. While this is a significant nondipole effect, it is not detected by experimental setups that lack an electron analyzer in the forward-backward plane or utilize extraction voltages to collect photoelectrons^{124, 131}. The current work makes use of an analyzer in the forward direction with respect to the incoming photon beam. Once again, it is unclear why the current results disagree with the findings of *Hemmers*⁷⁴, *Langhoff*⁷⁶, and *Guillemin*⁷⁷.

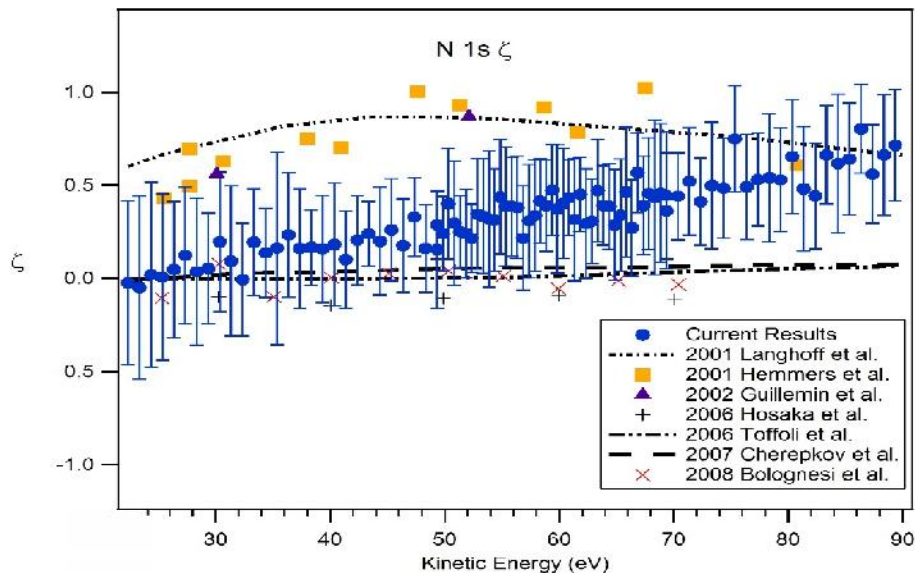


Figure 4.11. $N\ 1s\ \zeta(h\nu)$ in N_2 . The blue circles are present results, compared to previous experimental work from Hemmers⁷⁴ (red x marks), Guillemin⁷⁷, Hosaka¹²⁴ (orange squares), and Bolognesi¹³¹ (crosses), as well as *ab initio* calculations from Langhoff⁷⁶, density functional theory, single-center expansion (DFT-SCE) calculations from Toffoli¹²⁹, and relaxed core Hartree-Fock (RC-HF) calculations from Cherepkov¹³⁰.

In conclusion, the angular distribution parameters $\beta(h\nu)$ and $\zeta(h\nu)$ were experimentally determined for the $N\ 1s$ photoionization of molecular nitrogen between 22.0 – 90.0 eV photoelectron kinetic energy. The $\beta(h\nu)$ values were found to be in good agreement with previous measurements and calculations. However, the current $\zeta(h\nu)$ measurements differ from previous work. Our results only agree with Hemmers⁷⁴, Langhoff⁷⁶, and Guillemin⁷⁷ in that nondipole effects are present in this energy range, but the current work finds no evidence for a resonant nondipole effect around 60 eV. Regardless, it has been shown that first-order nondipole effects are significant in the case of $N\ 1s$ photoionization in N_2 . This is consistent with the idea that angular distributions are determined by how various multipole components of light interact with charge distributions (in this case electrons), and that, if nondipole effects are necessary in describing photoionization from atomic orbitals, they are also necessary for molecular orbitals.

Chapter 5 – Chiral Nondipole Effects in Carbon 1s Photoionization of Camphor

Chiral molecules have been studied using light since the pioneering work of Louis Pasteur in the mid-19th century. A molecule is said to be chiral if its geometric arrangement of atoms can take two mirror-image, non-superimposable forms. In this way, they are like hands, and the word ‘chiral’ comes from the Greek word for hand. An individual molecular arrangement is referred to as an enantiomer, and different nomenclatures exist for differentiating enantiomers. In this chapter, the R, S-nomenclature, also known as the Cahn-Ingold-Prelog rules¹³³, will be used.

Chiral molecules are important for their role in biology. Despite enantiomers having identical physical and chemical properties, only one enantiomer usually contributes to biological processes. Two well-known examples are amino acids, in which 18 out of the 20 standard amino acids are *S* enantiomers, and sugars, which, when utilized in living organisms, exist in the *R* configuration. This preference in life processes is not observed in the laboratory, as enantiomers are created in equal amounts (termed a *racemic mixture*) when synthesized from achiral reagents. This phenomenon is referred to as *homochirality*.

The origins of homochirality are unknown, but there exist competing theories. Findings of an *S* enantiomeric excess on the Murchison meteorite¹³⁶ motivated the idea of an extraterrestrial origin of homochirality, with the enantiomeric excess explained by the optical behavior of chiral molecules. Pasteur’s original work deduced that chiral molecules were

optically active, which means the plane of linearly polarized light is rotated as it passes through the sample. Individual enantiomers were also found to demonstrate differential absorption of left and right circularly polarized light, or circular dichroism. The circular dichroism effect was subsequently found in the angular distribution of photoelectrons^{102, 128, 137, 139, 140 - 146, 148 - 152, 154, 156, 158}. Circular dichroism in angular distributions (CDAD) results in a forward-backward asymmetry relative to the direction of photon propagation for photoelectrons that is dependent on enantiomer and the direction of the polarized light. The asymmetry is flipped if either the enantiomer or direction of circularly polarized light is changed. This work examines the possibility of a new form of *linear* dichroism, in which differences in angular distributions of photoelectrons are observed between *R* and *S* enantiomers in photoionization using linearly polarized light.

In order to observe any asymmetries in photoelectron angular distributions using linearly polarized light, approximations beyond the dipole approximation must be used. In the first-order correction to the dipole approximation, *Grum-Grzhimailo*⁵⁰ has proposed that angular distributions of photoelectrons from chiral molecules are determined according to Equation 1.8.

The chiral nondipole parameter $\varepsilon(h\nu)$ introduces a left-right asymmetry with respect to incoming photon propagation, much like the forward-backward asymmetry when using circularly polarized light. The goal of this work is to measure $\varepsilon(h\nu)$ in individual enantiomers. Any discrepancy in the values of $\varepsilon(h\nu)$ between enantiomers could be indicative of a new form of linear dichroism.

In order to determine the chiral nondipole parameter, $\beta(h\nu)$ for each enantiomer must be determined first. Based on the positions of the TOF analyzers (see Chapter 2), a ratio of electron counts in TOF analyzers 4 and 5 would depend only upon $\beta(h\nu)$. This work will focus on C 1s photoionization from *R*- and *S*-camphor. Camphor was chosen because it is readily available as pure enantiomers that do not undergo racemization when heated, which is required in order to introduce it into the chamber in the gas phase (see Chapter 2).

Photoelectron spectra within the energy range of 297.0 – 313.0 eV were collected separately for *R*- and *S*-camphor as described in Chapter 2. The pressure within the chamber was $\sim 10^{-6}$ Torr for each enantiomer and accelerating voltages between 3 – 18 V were applied in order to keep the photoelectrons at the same kinetic energy when detected by the microchannel plates. A sample C 1s photoelectron spectrum for both enantiomers collected at 301.0 eV are plotted together in Figure 5.1. The smaller peak is a result of C 1s photoionization from the carbonyl carbon, chemically shifted to a binding energy of 293.0 eV from the remaining nine carbons, which have a binding energy of ~ 290.5 eV¹³⁸. The two enantiomers show similar peak shapes and widths.

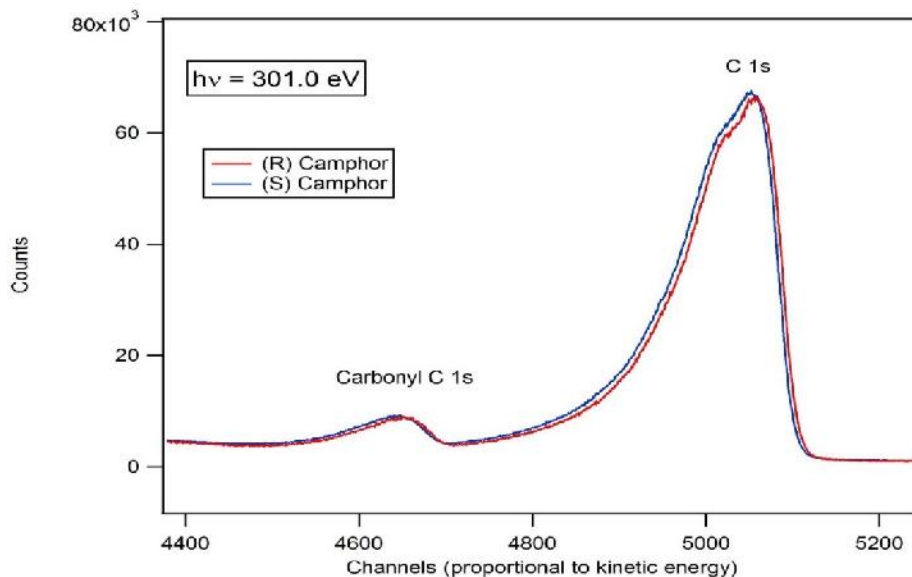


Figure 5.1. *R* and *S*-Camphor C 1s photoelectron spectrum at $h\nu = 301.0$ eV

Ratios of electron counts for TOF analyzers 4 and 5 are equivalent to the areas under the C 1s photoionization peaks for each respective analyzer. In this work, the C 1s peak area is the sum of carbonyl carbon peak plus the peak due to the remaining nine carbons. Previous measurements have focused on only the carbonyl carbon peak, and $\beta(h\nu)$ for carbonyl C 1s photoionization near threshold in camphor can be found in *Stener*¹²⁸ and *Nahon*¹⁴⁵.

The peak area ratios are related to $\beta(h\nu)$ according to the following expression:

$$\frac{Area\ TOF5}{Area\ TOF4} = \frac{T5}{T4} \left(\frac{1 - \frac{\beta(h\nu)}{2}}{1 + \beta(h\nu)} \right) \quad 5.1$$

where the areas refer to the combined C 1s photoelectron peak areas and $\frac{T5}{T4}$ is the transmission ratio as described in Chapter 2. Solving Equation 5.1 for $\beta(h\nu)$ gives:

$$\beta(h\nu) = \frac{\left(\frac{Area_{TOF5}}{Area_{TOF4}} \cdot \frac{T4}{T5} - \frac{TOF5}{TOF4} \right)}{\left(-\frac{1}{2} - \frac{Area_{TOF5}}{Area_{TOF4}} \cdot \frac{T4}{T5} \right)} \quad 5.2$$

In order to determine the transmission ratio measurements must be performed under the same conditions on a sample gas for which $\frac{T5}{T4}$ is known. For the purpose of this experiment, photoionization from the Ar 2p subshell was chosen because the energy difference between the Ar 2p_{3/2} and Ar 2p_{1/2} spin-orbit levels (2.2 eV)¹⁰⁷ was comparable to the $\frac{T5}{T4}$ difference due to the C 1s chemical shift of the carbonyl carbon in camphor, and the $\frac{5}{4}$ $\beta(h\nu)$ measurement has been calculated in the energy region of interest⁹¹. A plot of the calculated Ar 2p $\beta(h\nu)$ found in Chapter 4, Figure 4.4.

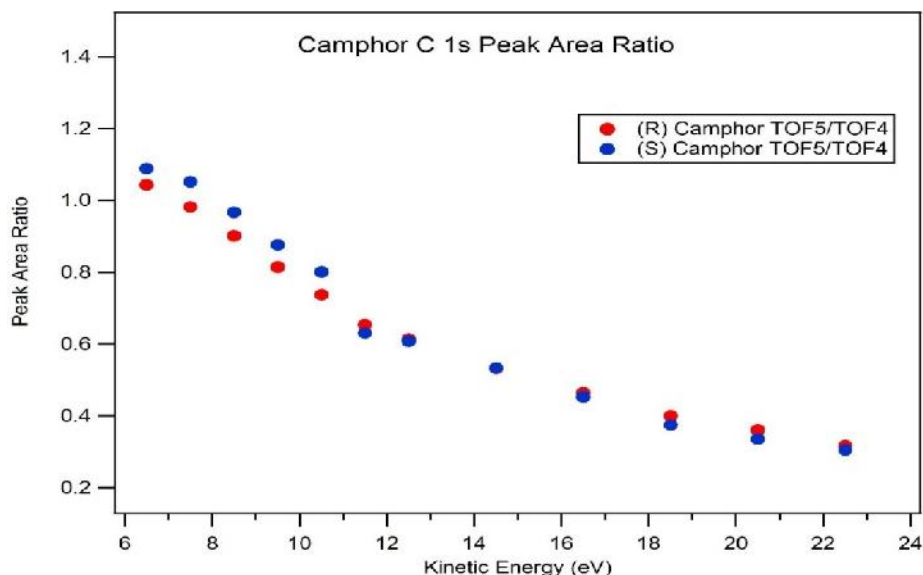


Figure 5.2. Camphor C 1s photoelectron peak area ratios

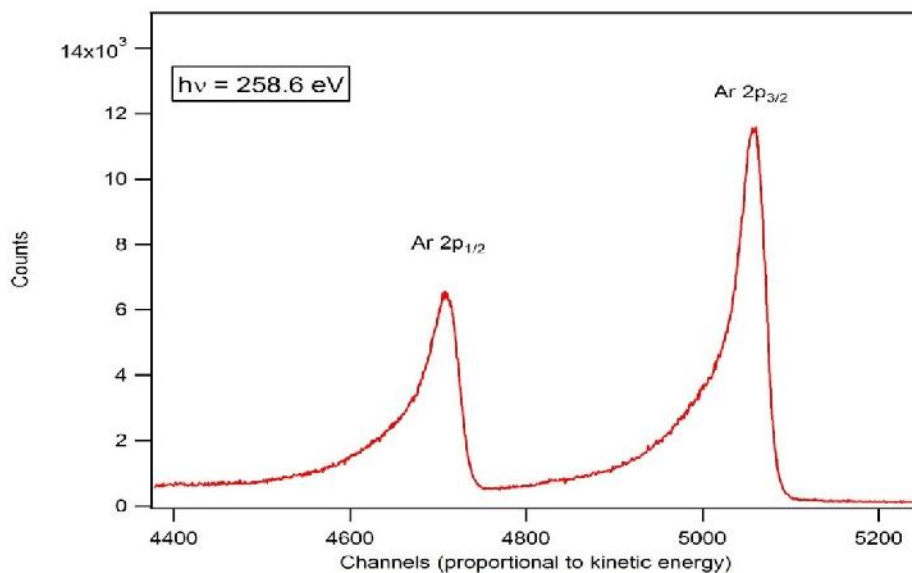


Figure 5.3. Ar 2p photoelectron spectrum at $h\nu = 258.6$ eV

Ar 2p photoelectron spectra were collected before each enantiomer of camphor within the photon energy range 254.6 – 270.6 eV, such that the Ar 2p photoelectron kinetic energies were equal to the camphor C 1s photoelectron kinetic energies. Other experimental conditions, such as gas pressure and applied accelerating voltages were the same as the camphor measurements. A sample Ar 2p spectrum taken at $h\nu = 258.6$ eV illustrating the spin-orbit splitting is shown in Figure 5.3.

Ratios of peak areas between TOF analyzers 5 and 4 are presented for each Ar 2p data set in Figure 5.4. The peak areas allow for the determination of the transmission ratio $\frac{T_5}{T_4}$ according to:

$$\frac{T5}{T4} = \left(\frac{1 + \beta(h\nu)}{1 - \frac{\beta(h\nu)}{2}} \right) \frac{Area\ TOF5}{Area\ TOF4'} \quad 5.3$$

where the areas and $\beta(h\nu)$ referring to the Ar 2p values. The resulting transmission ratios for each enantiomer are presented in Figure 5.5. The transmission ratios have been fit with smooth curves, as described in Chapter 3.

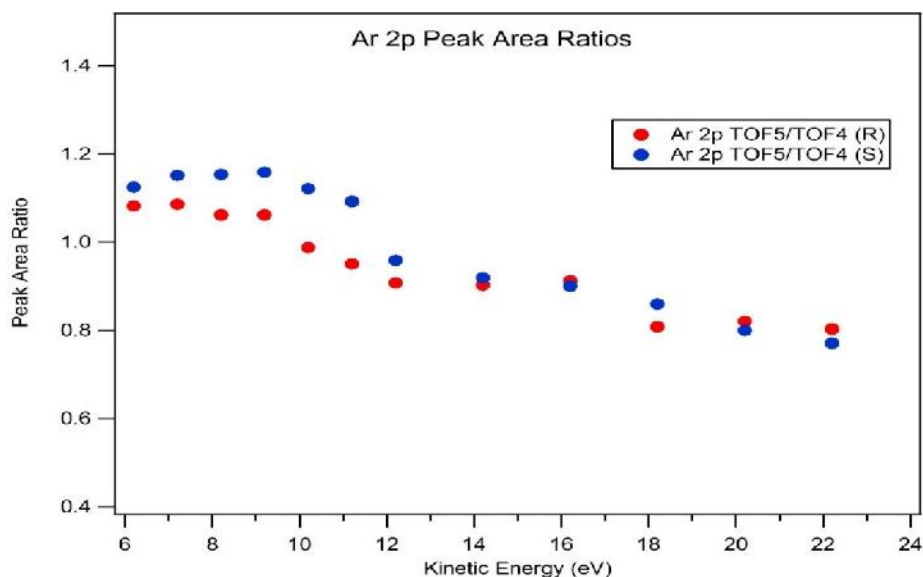


Figure 5.4. Ar 2p photoelectron peak area ratios. The (R) and (S) designations are indicative of which camphor enantiomer the particular ratios are calibrating.

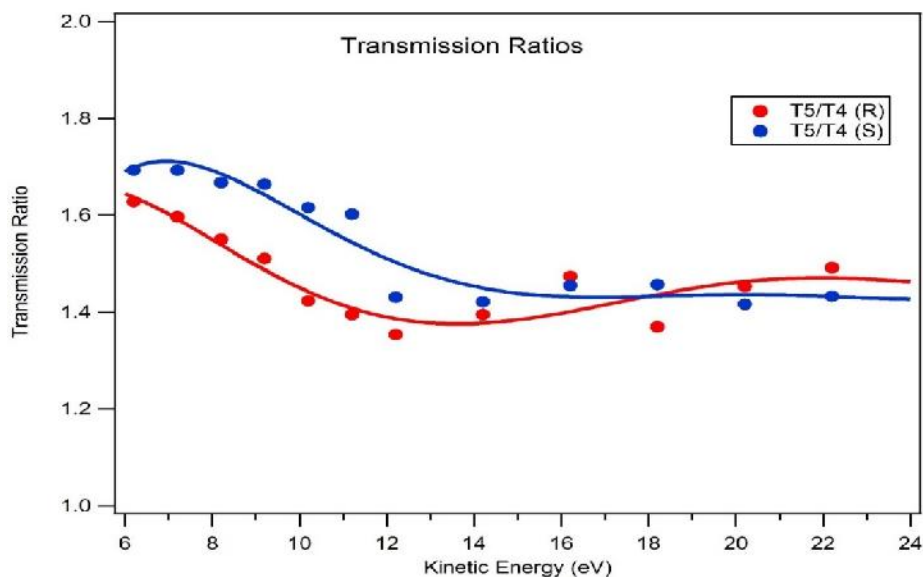


Figure 5.5. Time-of-flight (TOF) analyzer transmission ratios. The (R) and (S) indicate to which enantiomer of camphor each data set is applicable. The solid lines are the smooth fits that are described in the chapter.

The smooth fits for the transmission ratios were used to determine $\beta(h\nu)$ for each enantiomer according to Equation 5.2. The results are plotted in Figure 5.6. We find that $\beta(h\nu)$ increases steadily from $\sim 0.4 \pm 0.1$ to $\sim 1.0 \pm 0.1$ within this energy range for both enantiomers. The two enantiomers agree well in $\beta(h\nu)$, as they should, because enantiomers have identical chemical properties. The behavior of the $\beta(h\nu)$ curve is consistent with the general trend for core-level photoionization in molecules (see Chapter 1), in which $\beta(h\nu)$ is ~ 0 at threshold and increases to the asymptotic value $\beta(h\nu) = 2$ well above threshold. For details on the determination of error bars, see Chapters 3 and 4.

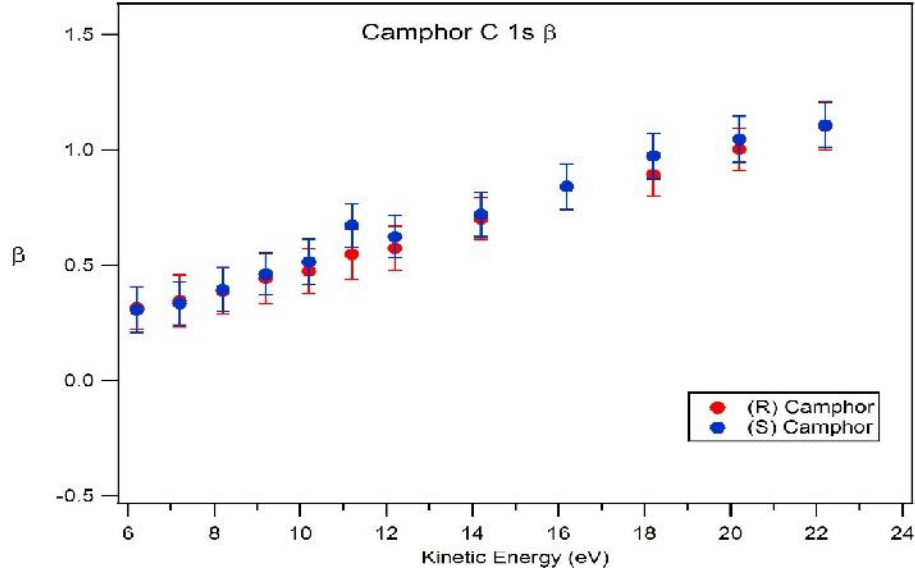


Figure 5.6. Camphor C 1s S.

Once $\beta(h\nu)$ has been determined, it is then possible to determine the chiral nondipole parameter $\varepsilon(h\nu)$ from the ratio of electrons between TOF analyzers 4 and 1 or TOF analyzers 5 and 1, according to the following expressions:

$$\frac{Area\ TOF4}{Area\ TOF1} = \frac{T4}{T1} \left(\frac{1 + \beta(h\nu)}{1 + \varepsilon(h\nu) \sin(-109.4^\circ)} \right) \quad 5.4$$

$$\frac{Area\ TOF5}{Area\ TOF1} = \frac{T5}{T1} \left(\frac{1 - \frac{\beta(h\nu)}{2}}{1 + \varepsilon(h\nu) \sin(-109.4^\circ)} \right) \quad 5.5$$

which are in reference to Equation 1.8. Rearrangement of Equations 5.4 and 5.5 give the following expressions for $\varepsilon(h\nu)$:

$$\varepsilon(h\nu) = \frac{(1 + \beta(h\nu)) \left(\frac{T4}{T1} * \frac{Area\ TOF1}{Area\ TOF4} \right) - 1}{\sin(-109.4^\circ)} \quad 5.6$$

$$\varepsilon(h\nu) = \frac{\left(1 - \frac{\beta(h\nu)}{2}\right) \left(\frac{T5}{T1} * \frac{Area\ TOF1}{Area\ TOF5}\right) - 1}{\sin^2(169.4^\circ)} \quad 5.7$$

The results for $\varepsilon(h\nu)$ for the enantiomers of camphor are presented in Figure 5.7. Error bars were determined in the same manner as $\beta(h\nu)$. We are able to conclude that since $\varepsilon(h\nu) \neq 0$, a chiral-specific nondipole effect is influencing the angular distribution of photoelectrons. However, the fact that $\varepsilon(h\nu)$ is the same within error for the two enantiomers suggests that chiral molecules do not exhibit linear dichroism in photoelectron angular distributions. However, this may be a result of studying randomly-oriented chiral molecules. In order for there to be a handedness to the electron distributions, there must be a way to define an orientation to the molecule. A definitive statement on linear dichroism could only be made if so-called “fixed-in-space” measurements were performed, as this would help define a molecular orientation at the moment of absorption.

In order to demonstrate the consequences of the chiral nondipole parameter, a sample plot of the photoelectron angular distribution probability amplitudes incorporating the $\varepsilon(h\nu)$ term is presented in Figure 5.8. The $\varepsilon(h\nu)$ and $\beta(h\nu)$ parameters chosen are from the measured results at 6.5 eV photoelectron kinetic energy, for which the $\varepsilon(h\nu)$ value is greatest.

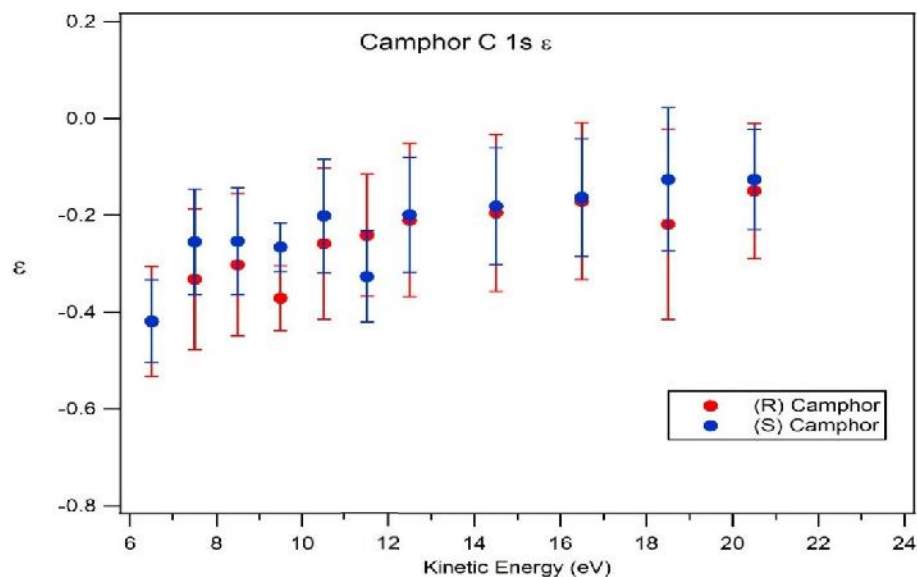


Figure 5.7 The chiral nondipole parameter ε plotted as a function of photoelectron kinetic energy for both the R (red) and S (blue) enantiomers of camphor

For comparison, a plot of the angular distribution probability amplitudes with the same $\beta(h\nu)$ value, but with no chiral nondipole effects ($\varepsilon = 0$) is included in the graph. In this plot, the polarization vector is at 0° and the direction of photon propagation is out of the page, towards the reader. From the figure, it is apparent that chirality has a dramatic influence on the angular distribution of photoelectrons, most readily observed as a left-right asymmetry along the polarization vector with respect to the photon propagation direction.

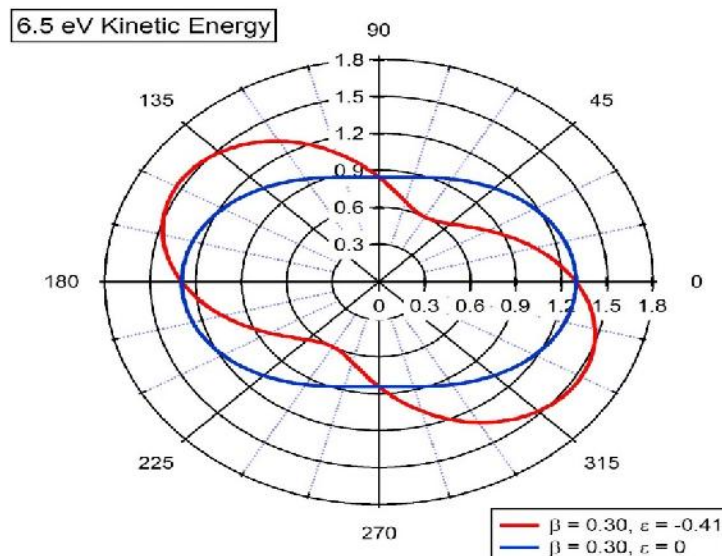


Figure 5.8 Plots of the angular distribution probability amplitudes corresponding to the lowest kinetic energy photoelectrons studied (6.5 eV) in both R and S Camphor. The red curve incorporates the measured chiral nondipole parameter's effects on the angular distribution, compared with the blue curve, which is the angular distribution probability assuming no chiral nondipole effects.

The placement of the TOF analyzers, as described in Chapter 2, allows for a way to test the current results. If no chiral nondipole effects are assumed, there are three ways to measure $\beta(h\nu)$: by taking ratios of TOF analyzers 5 and 4, analyzers 4 and 1, and analyzers 5 and 1. As can be seen in Figure 5.8, the ratio of TOF analyzers 5 and 4 is independent of chiral nondipole effects. However, due to the left-right asymmetry, the ratio of analyzers 4 and 1, will, when subjected to the analysis procedure outlined in Chapter 2, give different $\beta(h\nu)$ than the ratio of analyzers 5 and 1 for the same photoelectron kinetic energy. This test was performed, and the results are plotted in Figure 5.9.

We see a large difference in $\beta(h\nu)$ at lower photoelectron kinetic energy, depending on which analyzer ratio is used. This would imply that $\beta(h\nu)$ is angle-dependent, which could be

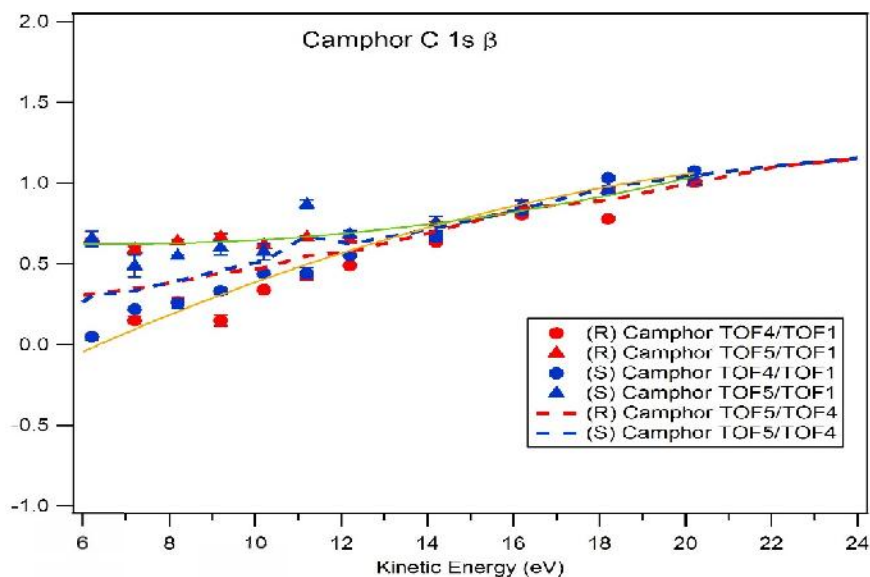


Figure 5.9. Plots of $\beta(h\nu)$ for C 1s photoionization of both enantiomers of camphor assuming no chiral nondipole effects. The blue and red circles are $\beta(h\nu)$ according to the ratio of TOF analyzers 4 and 1 for each enantiomer. The blue and red triangles are $\beta(h\nu)$ according to the ratio TOF analyzers 5 and 1. The blue and red dotted lines are $\beta(h\nu)$ according to the ratio of TOF analyzers 5 and 4, which are independent of chiral nondipole effects, and were presented in Figure 5.6. The green and orange solid lines are guides for the reader.

rationalized by a left-right asymmetry in the photoelectron angular distribution. Comparing Figure 5.9 with Figure 5.7, we see that the largest differences in $\beta(h\nu)$ occur for photoelectron kinetic energies with the largest $\varepsilon(h\nu)$ values, and decrease with as $\varepsilon(h\nu)$ decreases. This suggests that the magnitude of $\varepsilon(h\nu)$ is indicative of the degree of left-right asymmetry. And as can be seen from 5.8, values for $\varepsilon(h\nu)$ as small as -0.4 can result in large discrepancies between dipole and nondipole angular distributions. It is therefore imperative that any studies of chiral molecules using soft x-rays must include nondipole corrections.

It is also possible to test the existence of a chiral-specific nondipole effect by subjecting an achiral system to the same analysis methods. As an example, the chiral nondipole parameter for C 1s photoionization from carbon monoxide is plotted in Figure 5.10. Measurements on carbon dioxide allow for a comparison of $\varepsilon(h\nu)$ for chiral and achiral molecules in roughly the

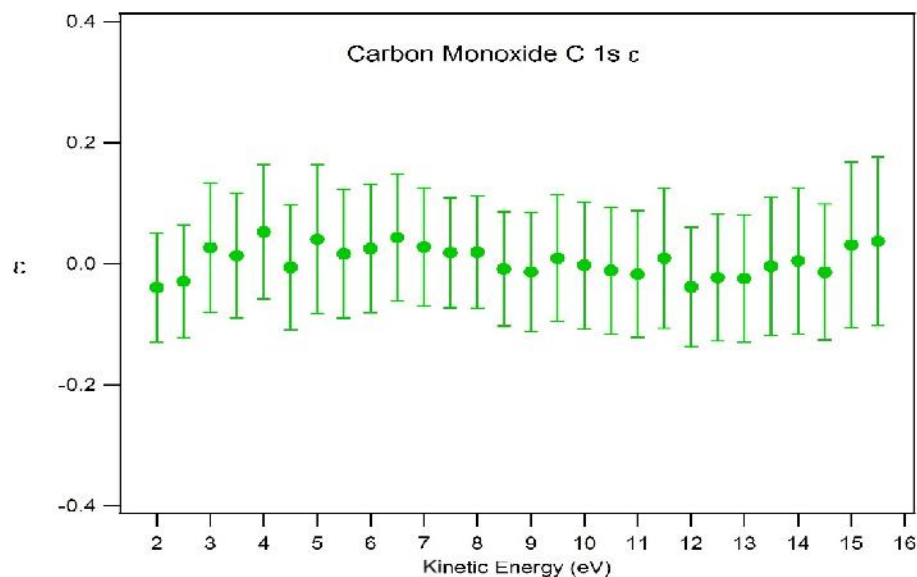


Figure 5.10. The chiral nondipole parameter ϵ plotted as a function of photoelectron kinetic energy for C 1s photoionization from carbon monoxide.

same photon energy region. Data for carbon monoxide was collected up to 16 eV above threshold in the same fashion as each enantiomer of camphor, and was also calibrated using Ar 2p. From the figure, we can see that $\epsilon(h\nu) = 0$ across the entire kinetic energy range measured. This is expected because CO is not a chiral molecule. These results help confirm that the current analysis procedure is valid for determining $\epsilon(h\nu)$, as well as provide evidence that chiral-specific nondipole effects are real.

In conclusion, for the first time, photoelectron angular distribution measurements of a chiral molecule using linearly polarized light were interpreted by incorporating chiral nondipole effects suggested by *Grum-Grzhimailo*⁵⁰. Electron time-of-flight measurements comparing electron counts in analyzers at specific angles for C 1s photoionization from individual camphor enantiomers demonstrated a left-right asymmetry in the angular distribution, and the degree of the asymmetry was reflected in the magnitude of a chiral-specific nondipole parameter, $\epsilon(h\nu)$.

The two enantiomers agreed in $\varepsilon(h\nu)$ for all photoelectron kinetic energies presented, which does not support the presence of linear dichroism in the angular distribution of photoelectrons from chiral molecules. Future studies, employing the “fixed-in-space” technique may reveal otherwise. Also, future measurements on different chiral molecules, as well as photoionization from other atoms and subshells within chiral molecules, would be helpful in determining the mechanism by which chirality influences the light-matter interaction.

Chapter 6 – Conclusions

It has become more common to utilize synchrotron radiation sources across many disciplines for a wide range of studies. For this reason, it is important to know the fundamentals of how synchrotron light, often linearly polarized and in the soft x-ray energy range, interacts with matter on the atomic scale. The goal of this work has been to examine the underlying assumptions in building a coherent and accurate model for describing the interaction of soft x-rays with matter.

Until the advent of third-generation synchrotron radiation sources, the prevailing assumption used in describing light-matter interactions was the dipole approximation. The dipole approximation, the simplest approximation, assuming light to be a uniform electric field, proved to be valid through the ultraviolet (UV) region, and was thought only to break down at high energies. With access to light with energies greater than UV made easier due to synchrotron radiation facilities, it became possible to test the limits of the dipole approximation.

Angular distributions of photoelectrons are sensitive to the properties of the incoming light, as well as electron correlations within the atom or molecule. Within the dipole approximation, angular distributions for randomly oriented atoms or molecules depend on only one measurable parameter, $\beta(h\nu)$. The distributions are symmetric with respect to both the photon propagation direction and the light's polarization vector. The relatively simple expression for the angular distribution allowed for the development of models which could predict values of $\beta(h\nu)$, given certain environments. Early measurements that resulted in

deviations from predicted $\beta(h\nu)$ values were attributed to relativistic effects, and were referred to as retardation. However, it was discovered shortly thereafter that the experimental deviations could be more accurately explained through the incorporation of first-order corrections to the dipole approximation, termed nondipole effects. Nondipole effects assumed a description of light that incorporated interference terms from higher-order multipole interactions. As a result, two additional parameters, $\delta(h\nu)$ and $\gamma(h\nu)$, were required to determine the angular distribution of photoelectrons. Nonzero values of these parameters account for forward-backward asymmetries with respect to photon propagation observed in photoelectron angular distributions.

This work has provided experimental evidence for the existence of nondipole effects in atomic (Xe 3*d*) and molecular (N 1*s* in N₂) photoionization. Current results were compared with previous measurements and calculations. For Xe 3*d*, effects attributed to interchannel coupling have been found in both the dipole and nondipole angular distribution parameters that have been absent in all previous measurements and calculations. However, this indicates one of the strengths of measurements such as this, as it is hoped that by investigating this discrepancy, the most accurate model for electron correlations in systems like Xe can be obtained.

A similar situation exists for N₂, where previous measurements and calculations disagree over the presence of nondipole effects. Within this work, four possible explanations have been given in an attempt to model the photoionization of core electrons from molecular nitrogen. The first explanation suggests that large resonant nondipole effects depend upon the bond lengths of various vibrational states. The second proposes that nondipole effects between opposite symmetry states cancel, resulting in no observable nondipole effects. The third

suggests that nondipole effects are not necessary in describing N₂ photoionization, and the last finding, from the current work, suggests the presence of nondipole effects, but does not see the effect as a result of bond-length dependence in nondipole angular distribution parameters.

The experimental technique described in this work was shown to be a valuable asset in testing models of the light-matter interaction. Over a decade ago, it was proposed that the lack of symmetry in chiral molecules could be responsible for a unique nondipole effect when using linearly polarized light. It had already been established that chiral molecules exhibit circular dichroism in photoelectron angular distributions within the dipole approximation. The current experiment investigated a possible new form of linear dichroism as a result of nondipole effects. And while, according to the results from camphor, there is no evidence supporting a new form of linear dichroism, the chiral-specific nondipole effect was found to be real. A major implication of this effect is that any measurements made with linearly polarized light that assume the dipole approximation could give inaccurate results. This is all the more vital as research continues on the unsolved origins of homochirality.

It is important to note that tried and tested experimental techniques on well-studied systems are still capable of providing quality answers to fundamental questions about basic processes in the universe. Measuring angular distributions of photoelectrons is a valuable technique that only becomes more relevant as systems become more complex, if we truly desire a basic understanding of how things work on an atomic scale.

References

- [1] Einstein, A. On a heuristic viewpoint concerning the production and transformation of light. *Annalen der Physik* **1905**, 17, 132-148.
- [2] Yang, C. N. On the Angular Distribution in Nuclear Reactions and Coincidence Measurements. *Physical Review* **1948**, 74, 764-772.
- [3] Burhop, E.H.S. *The Auger Effect and Other Radiationless Transitions*, 1st ed.; Cambridge University Press: Cambridge, U.K., 1952.
- [4] Bethe, H. A.; Salpeter, E. E. *Quantum Mechanics of One- and Two-Electron Atoms*, 1st ed.; Springer : Berlin, 1957.
- [5] Cooper, J.W. Photoionization from Outer Atomic Subshells. A Model Study. *Physical Review* **1962**, 128, 681-693.
- [6] Cooper, J.; Zare, R. N. Angular Distribution of Photoelectrons. *Journal of Chemical Physics* **1968**, 48, 942-943.
- [7] Tully, J. C.; Berry, R. S.; Dalton, B. J. Angular Distribution of Molecular Photoelectrons. *Physical Review* **1968**, 176, 95-105.
- [8] Cooper, J. W.; Manson, S. T. Photo-Ionization in the Soft X-Ray Range: Angular Distributions of Photoelectrons and Interpretation in Terms of Subshell Structure. *Physical Review* **1969**, 177, 157-163.
- [9] Krause, M. O. Photo-Ionization of Krypton Between 300 and 1500 eV. Relative Subshell Cross Sections and Angular Distributions of Photoelectrons. *Physical Review* **1969**, 177, 151-157.
- [10] Fano, U.; Dill, D. Angular Momentum Transfer in the Theory of Angular Distributions. *Physical Review A* **1972**, 6, 185-192.
- [11] Wuilleumier, F.; Krause, M. O. Photoionization of neon between 100 and 2000 eV: Single and multiple processes, angular distributions, and subshell cross sections. *Physical Review A* **1974**, 10, 242-258.
- [12] Kabachnik, N. M.; Sazhina, I. P. Angular distribution and polarization of photoelectrons in the region of resonances. *Journal of Physics B: Atomic and Molecular Physics* **1976**, 9, 1681-1697.

- [13] Ritchie, B. Theory of the angular distribution of photoelectrons ejected from optically active molecules and molecular negative ions. *Physical Review A* **1976**, *13*, 1411-1415.
- [14] Ron, A.; Pratt, R. H.; Tseng, H. K. Limitations on the Validity of the Non-Relativistic Dipole Approximation for Photoelectron Angular Distributions. *Chemical Physics Letters* **1977**, *47*, 377-379.
- [15] Tseng, H. K.; Pratt, R. H.; Yu, S.; Ron, A. Photoelectron angular distributions. *Physical Review A* **1978**, *17*, 1061-1079.
- [16] Wang, M. S.; Kim, Y. S.; Pratt, R. H.; Ron, A. Observation of zeros and amplification of quadrupole-matrix-element contributions to photoelectron angular distributions. *Physical Review A* **1982**, *25*, 857-861.
- [17] Bechler, A.; Pratt, R. H. Higher retardation and multipole corrections to the dipole angular distribution of 1s photoelectrons at low energies. *Physical Review A* **1989**, *39*, 1774-1779.
- [18] Bechler, A.; Pratt, R. H. Higher multipole and retardation corrections to the dipole angular distributions of L-shell photoelectrons ejected by polarized photons. *Physical Review A* **1990**, *42*, 6400-6413.
- [19] Cooper, J. W. Multipole corrections to the angular distribution of photoelectrons at low energies. *Physical Review A* **1990**, *42*, 6942-6945.
- [20] Scofield, J. H. Angular distribution of photoelectrons from polarized X-rays. *Physica Scripta* **1990**, *41*, 59-62.
- [21] Cooper, J. W. Formulas Photoelectron-angular-distribution parameters for rare-gas subshells. *Physical Review A* **1993**, *47*, 1841-1851.
- [22] Ron, A.; Goldberg, I. B.; Stein, J.; Manson, S. T.; Pratt, R. H.; Yin, R. Y. Relativistic, retardation, and multipole effects in photoionization cross sections: Z, n, and l dependence. *Physical Review A* **1994**, *50*, 1312-1320.
- [23] Krässig, B.; Jung, M.; Gemmell, D. S.; Kanter, E. P.; LeBrun, T.; Southworth, S. H.; Young, L. Nondipolar Asymmetries of Photoelectron Angular Distributions. *Physical Review Letters* **1995**, *75*, 4736-4739.
- [24] Pratt, R. H.; LaJohn, L. The need to include multipole effects beyond the dipole approximation in the description of photoionization both at nonrelativistic and

relativistic energies. *Nuclear Instruments and Methods in Physics Research B* **1995**, *99*, 136-139.

- [25] Seaton, M. J. Momentum transfer in photo-ionization processes. *Journal of Physics B: Atomic, Molecular and Optical Physics* **1995**, *28*, 3185-3196.
- [26] Jung, M.; Krässig, B.; Gemmell, D. S.; Kanter, E. P.; LeBrun, T.; Southworth, S. H.; Young, L. Experimental determination of nondipolar angular distribution parameters for photoionization in the Ar K and Kr L shells. *Physical Review A* **1996**, *54*, 2127-2136.
- [27] King, G. C.; Schartner, K. - H. Resonances and Near-Threshold Processes. In VUV and Soft X-Ray Photoionization; Becker, U.; Shirley, D.A., Ed.; Plenum Press: New York, 1996; pp 355-400.
- [28] Kutzner, M. Many-Electron Effects in Photoionization. In VUV and Soft X-Ray Photoionization; Becker, U.; Shirley, D.A., Ed.; Plenum Press: New York, 1996; pp 47-80.
- [29] Shaw, P. S.; Southworth, S. H. Measuring nondipolar asymmetries of photoelectron angular distributions. *Physical Review A* **1996**, *54*, 1463-1472.
- [30] Dias, E. W. B.; Chakraborty, H. S.; Deshmukh, P. C.; Manson, S. T.; Hemmers, O.; Glans, P.; Hansen, D.; Wang, H.; Whitfield, S. B.; Lindle, D. W.; Wehlitz, R.; Levin, J. C.; Sellin, I. A. Breakdown of the Independent Particle Approximation in High-Energy Photoionization. *Physical Review Letters* **1997**, *78*, 4553-4556.
- [31] Hemmers, O.; Fisher, G.; Glans, P.; Hansen, D. L.; Wang, H.; Whitfield, S. B.; Wehlitz, R.; Levin, J. C.; Sellin, I. A.; Perera, R. C. C.; Dias, E. W. B.; Chakraborty, H. S.; Deshmukh, P. C.; Manson, S. T.; Lindle, D. W. Beyond the dipole approximation: angular-distribution effects in valence photoemission. *Journal of Physics B: Atomic, Molecular and Optical Physics* **1997**, *30*, L727-L733.
- [32] Martin, N. L. S.; Thompson, D. B.; Bauman, R. P.; Caldwell, C. D.; Krause, M. O.; Frigo, S. P.; Wilson, M. Electric-Dipole–Quadrupole Interference of Overlapping Autoionizing Levels in Photoelectron Energy Spectra. *Physical Review Letters* **1998**, *81*, 1199-1202.
- [33] Amusia, M. Y.; Baltenkov, A. S.; Felfli, Z.; Msezane, A. Z. Large nondipole correlation effects near atomic photoionization thresholds. *Physical Review A* **1999**, *59*, R2544-R2547.
- [34] Dolmatov, V. K.; Manson, S. T. Enhanced Nondipole Effects in Low Energy Photoionization. *Physical Review Letters* **1999**, *83*, 939-942.

- [35] Johnson, W. R.; Derevianko, A.; Cheng, K. T.; Dolmatov, V. K.; Manson, S. T. Nondipole effects in the photoionization of neon: Random-phase approximation. *Physical Review A* **1999**, *59*, 3609-3613.
- [36] Kutzner, M.; Rose, M. A theoretical investigation of K-shell photoionization in neon. *Journal of Physics B: Atomic, Molecular and Optical Physics* **1999**, *32*, 123-127.
- [37] Lindle, D. W.; Hemmers, O. Breakdown of the dipole approximation in soft-X-ray photoemission. *Journal of Electron Spectroscopy and Related Phenomena* **1999**, *100*, 297-311.
- [38] Piancastelli, M. N. The neverending story of shape resonances. *Journal of Electron Spectroscopy and Related Phenomena* **1999**, *100*, 167-190.
- [39] Altun, Z.; Manson, S. T. Photoelectron angular distributions of ns subshells of open-shell atoms as indicators of interchannel coupling: Sc 4s photoionization. *Physical Review A* **2000**, *61*, 030702(R) 1-4.
- [40] Connerade, J. P.; Dolmatov, V. K.; Manson, S. T. Controlled strong non-dipole effects in photoionization of confined atoms. *Journal of Physics B: Atomic, Molecular and Optical Physics* **2000**, *33*, L275-L282.
- [41] Derevianko, A.; Hemmers, O.; Oblad, S.; Glans, P.; Wang, H.; Whitfield, S. B.; Wehlitz, R.; Sellin, I. A.; Johnson, W. R.; Lindle, D. W. Electric-Octupole and Pure-Electric Quadrupole Effects in Soft X-ray Photoemission. *Physical Review Letters* **2000**, *84*, 2116-2119.
- [42] Nefedov, V. I.; Yarzhemsky, V. G.; Nefedova, I. S.; Trzhaskovskaya, M. B. Systematics of the behavior of nondipolar photoelectron angular distribution parameter γ . *Journal of Electron Spectroscopy and Related Phenomena* **2000**, *113*, 91-95.
- [43] Nefedov, V. I.; Yarzhemsky, V. G.; Nefedova, I. S.; Trzhaskovskaya, M. B.; Band, I.M. The influence of non-dipolar transitions on the angular photoelectron distribution. *Journal of Electron Spectroscopy and Related Phenomena* **2000**, *107*, 123-130.
- [44] Chakraborty, H. S.; Hansen, D. L.; Hemmers, O.; Deshmukh, P. C.; Focke, P.; Sellin, I. A.; Heske, C.; Lindle, D. W.; Manson, S. T. Interchannel coupling in the photoionization of the M shell of Kr well above threshold: Experiment and theory. *Physical Review A* **2001**, *63*, 042708 1-4.
- [45] Grum-Grzhimailo, A. N. Non-dipole effects in magnetic dichroism in atomic photoionization. *Journal of Physics B: Atomic, Molecular and Optical Physics* **2001**, *34*, L359-L365.

- [46] Hemmers, O.; Blackburn, M.; Goddard, T.; Glans, P.; Wang, H.; Whitfield, S. B.; Wehlitz, R.; Sellin, I. A.; Lindle, D. W. Dipole and nondipole angular-distribution effects in valence photoemission from neon. *Journal of Electron Spectroscopy and Related Phenomena* **2002**, 123, 257-264.
- [47] Amusia, M. Ya; Baltenkov, A. S.; Chernysheva, L. V.; Felfli, Z.; Manson, S. T.; Msezane, A. Z. Correlation structure in nondipole photoionization. *Physical Review A* **2003**, 67, 060702(R) 1-4.
- [48] Cherepkov, N. A.; Semenov, S. K.; Drescher, M.; Heinzmann, U. Resonance enhancement of non-dipole effects in spin polarization of atomic photoelectrons. *Journal of Physics B: Atomic, Molecular and Optical Physics* **2003**, 36, 3063-3078.
- [49] Dolmatov, V. K.; Baltenkov, A. S.; Manson, S. T. Enhanced nondipole effects in photoelectron angular distributions near giant dipole autoionizing resonances in atoms. *Physical Review A* **2003**, 67, 062714 1-6.
- [50] Grum-Grzhimailo, A. N. On the angular distributions in molecular photoionization beyond the dipole approximation. *Journal of Physics B: Atomic, Molecular and Optical Physics* **2003**, 36, 2385-2407.
- [51] Kanter, E. P.; Krässig, B.; Southworth, S. H.; Guillemin, R.; Hemmers, O.; Lindle, D. W.; Wehlitz, R.; Amusia, M. Ya; Chernysheva, L. V.; Martin, N. L. S. E1-E2 interference in the vuv photoionization of He. *Physical Review A* **2003**, 68, 012714 1-10.
- [52] Krässig, B.; Bilheux, J. – C.; Dunford, R. W.; Gemmell, D. S.; Hasegawa, S.; Kanter, E. P.; Southworth, S. H.; Young, L. Nondipole asymmetries of Kr 1s photoelectrons. *Physical Review A* **2003**, 67, 022707 1-7.
- [53] Hemmers, O.; Guillemin, R.; Lindle, D. W. Nondipole effects in soft X-ray photoemission. *Radiation Physics and Chemistry* **2004**, 70, 123-147.
- [54] Dolmatov, V. K. B., D; Manson, S. T. Gigantic enhancement of atomic nondipole effects: The 3s \rightarrow 3d resonance in Ca. *Physical Review. A* **2005**, 72, 022718 1-5.
- [55] Guillemin, R.; Hemmers, O.; Lindle, D. W.; Manson, S. T. Experimental investigation of nondipole effects in photoemission at the advanced light source. *Radiation Physics and Chemistry* **2005**, 73, 311-327.

- [56] Seabra, G.; Ortiz, J.; Kaplan, I. Molecular photoionization cross sections in electron propagator theory: Angular distributions beyond the dipole approximation. *Journal of Chemical Physics* **2005**, *123*, 114105 1-6.
- [57] Guillemin, R.; Hemmers, O.; Lindle, D. W.; Manson, S. T. Experimental investigation of nondipole effects in photoemission at the advanced light source. *Radiation Physics and Chemistry* **2006**, *75*, 2258-2274.
- [58] Southworth, S. H.; Dunford, R. W.; Kanter, E. P.; Krässig, B.; Young, L.; LaJohn, L. A.; Pratt, R. H. Nondipole asymmetries of K-shell photoelectrons of Kr, Br₂, and BrCF₃. *Radiation Physics and Chemistry* **2006**, *75*, 1574-1577.
- [59] Dolmatov, V. K. Strong final-state term dependence of nondipole photoelectron angular distributions from half-filled shell atoms. *Physical Review. A* **2006**, *74*, 032705 1-7.
- [60] Banerjee, T.; Deshmukh, P. C.; Manson, S. T. Krypton E2 photoionization cross-section and angular distribution of photoelectrons. *Journal of Physics: Conference Series* **2007**, *80*, 012001 1-8.
- [61] Banerjee, T.; Deshmukh, P. C.; Manson, S. T. Dipole and quadrupole Cooper minima and their effects on dipole and nondipole photoelectron angular distributions in Hg 6s. *Physical Review A* **2007**, *75*, 042701 1-8.
- [62] Dolmatov, V. K.; Guler, E.; Manson, S. T. "Reading" the photoelectron β -parameter spectrum in a resonance region. *Physical Review A* **2007**, *76*, 032704 1-5.
- [63] Deshmukh, P. C.; Banerjee, T.; Varma, H. R.; Hemmers, O.; Guillemin, R.; Rolles, D.; Wolska, A.; Yu, S. W.; Lindle, D. W.; Johnson, W. R.; Manson, S. T. Theoretical and experimental demonstrations of the existence of quadrupole Cooper minima. *Journal of Physics B: Atomic, Molecular and Optical Physics* **2008**, *41*, 021002 1-5.
- [64] Nefedov, V.; Yarzhemsky, V.; Trzhaskovskaya, M. The influence of relaxation and nondipole effects on the intensity of X-ray photoelectron spectra. *Bulletin of the Russian Academy of Sciences: Physics* **2008**, *72*, 423-428.
- [65] Toffoli, D.; Decleva, P. A multicentric approach to the calculation of nondipolar effects in molecular photoemission. *The Journal of Chemical Physics* **2008**, *128*, 234101 1-13.
- [66] Toffoli, D.; Decleva, P. Nondipolar effects in the photoionization dynamics of carbon tetrafluoride. *Physical Review A* **2008**, *78*, 063402 1-10.

- [67] Grum-Grzhimailo, A. N.; Meyer, M. Magnetic dichroism in atomic core level photoemission. *The European Physical Journal: Special Topics* **2009**, *169*, 43-50.
- [68] Argenti, L.; Moccia, R. Nondipole effects in helium photoionization. *Journal of Physics B: Atomic, Molecular and Optical Physics* **2010**, *43*, 235006, 1-8.
- [69] Ricz, S.; Ricsóka, T.; Holste, K.; Borovik Jr., A.; Bernhardt, D.; Schippers, S.; Kövér, Á.; Varga, D.; Müller, A. Interference effect in the dipole and nondipole anisotropy parameters of the Kr 4 p photoelectrons in the vicinity of the Kr $(3d)^{-1} \rightarrow np$ resonant excitations. *Physical Review A* **2010**, *81*, 043416 1-7.
- [70] Pradhan, G. B.; Jose, J.; Deshmukh, P. C.; LaJohn, L. A.; Pratt, R. H.; Manson, S. T. Cooper minima: a window on nondipole photoionization at low energy. *Journal of Physics B: Atomic, Molecular and Optical Physics* **2011**, *44*, 201001 1-6.
- [71] Hemmers, O.; Whitfield, S. B.; Glans, P.; Wang, H.; Lindle, D. W.; Wehlitz, R.; Sellin, I. A. High-resolution electron time-of-flight apparatus for the soft x-ray region. *Review of Scientific Instruments* **1998**, *69*, 3809-3817.
- [72] Hansen, D. L.; Hemmers, O.; Wang, H.; Lindle, D. W.; Focke, P.; Sellin, I. A.; Heske, C.; Chakraborty, H. S.; Deshmukh, P. C.; Manson, S. T. Validity of the independent-particle approximation in x-ray photoemission: The exception, not the rule. *Physical Review A* **1999**, *60*, R2641-R2644.
- [73] Arce, J. C.; Sheehy, J. A.; Langhoff, P. W.; Hemmers, O.; Wang, H.; Focke, P.; Sellin, I. A.; Lindle, D. W. On the angular distributions of molecular photoelectrons: dipole cross-sections for fixed-in-space and randomly oriented molecules. *Chemical Physics Letters* **2001**, *346*, 341-346.
- [74] Hemmers, O.; Manson, S. T.; Sant'Anna, M. M.; Focke, P.; Wang, H.; Sellin, I. A.; Lindle, D. W. Relativistic effects on interchannel coupling in atomic photoionization: The photoelectron angular distribution of Xe 5s. *Physical Review A* **2001**, *64*, 022507 1-3.
- [75] Hemmers, O.; Wang, H.; Focke, P.; Sellin, I. A.; Lindle, D. W.; Arce, J. C.; Sheehy, J. A.; Langhoff, P. W. Large Nondipole Effects in the Angular Distributions of K-Shell Photoelectrons from Molecular Nitrogen. *Physical Review Letters* **2001**, *87*, 273003 1-4.
- [76] Langhoff, P. W.; Arce, J. C.; Sheehy, J. A.; Hemmers, O.; Wang, H.; Focke, P.; Sellin, I. A.; Lindle, D. W. On the angular distributions of electrons photoejected from fixed-in-space and randomly oriented molecules. *Journal of Electron Spectroscopy and Related Phenomena* **2001**, *114*, 23-32.

- [77] Guillemin, R.; Hemmers, O.; Lindle, D. W.; Shigemasa, E.; Le Guen, K.; Ceolin, D.; Miron, C.; Leclercq, N.; Morin, P.; Simon, M.; Langhoff, P. W. Nondipolar electron angular distributions from fixed-in-space molecules. *Physical Review Letters* **2002**, *89*, 033002 1-4.
- [78] Hemmers, O.; Guillemin, R.; Kanter, E. P.; Krässig, B.; Lindle, D. W.; Southworth, S. H.; Wehlitz, R.; Baker, J.; Hudson, A.; Lotrakul, M.; Rolles, D.; Stolte, W. C.; Tran, I. C.; Wolska, A.; Yu, S. W.; Amusia, M. Ya; Cheng, K. T.; Chernysheva, L. V.; Johnson, W. R.; Manson, S. T. Dramatic nondipole effects in low-energy photoionization: Experimental and theoretical study of Xe 5s. *Physical Review Letters* **2003**, *91*, 530021-530024.
- [79] Hemmers, O.; Guillemin, R.; Rolles, D.; Wolska, A.; Lindle, D. W.; Kanter, E. P.; Krässig, B.; Southworth, S. H.; Wehlitz, R.; Langhoff, P. W.; McKoy, V.; Zimmermann, B. Nondipole effects in molecular nitrogen valence shell photoionization. *Journal of Electron Spectroscopy and Related Phenomena* **2005**, *144*, 155-156.
- [80] Hemmers, O.; Guillemin, R.; Rolles, D.; Wolska, A.; Lindle, D. W.; Kanter, E. P.; Krässig, B.; Southworth, S. H.; Wehlitz, R.; Zimmermann, B.; McKoy, V.; Langhoff, P. W. Low-energy nondipole effects in molecular nitrogen valence-shell photoionization. *Physical Review Letters* **2006**, *97*, 103006 1-4.
- [81] Lawrence Berkeley National Lab. Advanced Light Source: Beamline 8.0.1. <https://www-als.lbl.gov/index.php/ring-leaders/115-801.html> (Accessed March 22, 2016).
- [82] Torop, L.; Morton, J.; West, J. B. The angular distribution of photoelectrons from xenon. *Journal of Physics B: Atomic and Molecular Physics* **1976**, *9*, 2035-2041.
- [83] Sonntag, B.; Nagata, T.; Sato, Y.; Satow, Y.; Yagishita, A.; Yanagihara, M. Collapse of the f-symmetric final-state wavefunction in the 3d excitation spectra of atomic Xe, Cs and Ba. *Journal of Physics B: Atomic and Molecular Physics* **1984**, *17*, L55-L58.
- [84] Amusia, M. Y.; Ivanov, V. K.; Kupchenko, V. A. The effect of atomic rearrangement on the photoionisation cross section for 3d subshells of the isoelectronic Xe series. *Journal of Physics B: Atomic and Molecular Physics* **1985**, *18*, 3871-3879.
- [85] Becker, U.; Kerkhoff, H. G.; Kupsch, M.; Langer, B.; Szostak, D.; Wehlitz, R. Photoionization of Xenon with Soft X-Rays. *Le Journal de Physique Colloques* **1987**, *48*, C9 497-500.
- [86] Lindle, D. W.; Ferrett, T. A.; Heimann, P. A.; Shirley, D. A. Photoemission from Xe in the vicinity of the 4d Cooper minimum. *Physical Review A* **1988**, *37*, 3808-3812.

- [87] Becker, U.; Szostak, D.; Kerkhoff, H. G.; Kupsch, M.; Langer, B.; Wehlitz, R.; Yagishita, A.; Hayaishi, T. Subshell photoionization of Xe between 40 and 1000 eV. *Physical Review A* **1989**, 39, 3902-3911.
- [88] Lagutin, B. M.; Petrov, I. D.; Sukhorukov, V. L.; Whitfield, S. B.; Langer, B.; Viefhaus, J.; Wehlitz, R.; Berrah, N.; Mahler, W.; Becker, U. Cross sections and angular distributions of the photoelectron correlation satellites of the Xe atom. *Journal of Physics B: Atomic, Molecular and Optical Physics* **1996**, 29, 937-976.
- [89] Cubric, D.; Thompson, D. B.; Cooper, D. R.; King, G. C.; Read, F. H. A study of photoelectron angular distributions in xenon using a new magnetic angle-changing technique. *Journal of Physics B: Atomic, Molecular and Optical Physics* **1997**, 30, L857-L864.
- [90] Arp, U.; Iemura, K.; Kutluk, G.; Nagata, T.; Yagi, S.; Yagishita, A. 3d photoionization of Xe, Cs and Ba and the collapse of the 4f wavefunction. *Journal of Physics B: Atomic, Molecular and Optical Physics* **1999**, 32, 1295-1304.
- [91] Derevianko, A.; Johnson, W. R.; Cheng, K. T. Non-Dipole Effects in Photoelectron Angular Distributions for Rare Gas Atoms. *Atomic Data and Nuclear Data Tables* **1999**, 73, 153-211.
- [92] Kivimäki, A.; Hergenhahn, U.; Kempgens, B.; Hentges, R.; Piancastelli, M. N.; Maier, K.; Rüdel, A.; Tulkki, J. J.; Bradshaw, A. M. Near-threshold study of Xe 3d photoionization. *Physical Review A* **2000**, 63, 012716 1-7.
- [93] Amusia, M. Y.; Baltenkov, A. S.; Chernysheva, L. V.; Felfli, Z.; Msezane, A. Z. Nondipole parameters in angular distributions of electrons in photoionization of noble-gas atoms. *Physical Review A* **2001**, 63, 052506 1-8.
- [94] Johnson, W. R. Strong nondipole effects in low-energy photoionization of the 5s and 5p subshells of xenon. *Physical Review A* **2001**, 63, 022504 1-4.
- [95] Radojević, V.; Davidović, D. M.; Amusia, M. Y. Near-threshold photoionization of the Xe 3d spin-orbit doublet: Relativistic, relaxation, and intershell interaction effects. *Physical Review A* **2003**, 67, 022719 1-6.
- [96] Ricz, S.; Sankari, R.; Kövér, Á.; Jurvansuu, M.; Varga, D.; Nikkinen, J.; Ricsoka, T.; Aksela, H.; Aksela, S. Strong nondipole effect created by multielectron correlation in 5s photoionization of xenon. *Physical Review A* **2003**, 67, 012712 1-4.

- [97] Toffoli, D.; Stener, M.; Decleva, P. 3d photoionization along the xenon isoelectronic sequence. *Journal of Physics B: Atomic, Molecular and Optical Physics* **2003**, *36*, 3097-3118.
- [98] Amusia, M. Y.; Baltenkov, A. S.; Chernysheva, L. V.; Felfli, Z.; Manson, S. T.; Msezane, A. Z. Effects of spin-orbit activated interchannel coupling on dipole photoelectron angular distribution asymmetry parameters. *Journal of Physics B: Atomic, Molecular and Optical Physics* **2004**, *37*, 937-944.
- [99] Hemmers, O.; Guillemin, R.; Rolles, D.; Wolska, A.; Lindle, D. W.; Cheng, K. T.; Johnson, W. R.; Zhou, H. L.; Manson, S. T. Nondipole effects in the photoionization of Xe 4d_{5/2} and 4d_{3/2}: evidence for quadrupole satellites. *Physical Review Letters* **2004**, *93*, 113001 1-4.
- [100] Deshmukh, P. C.; Banerjee, T.; Sunanda, K. P.; Varma, H. R. Interchannel coupling effects on non-dipole photoionization parameters. *Radiation Physics and Chemistry* **2006**, *75*, 2211-2220.
- [101] Amusia, M. Ya; Baltenkov, A. S.; Chernysheva, L. V. Photoionization of Xe 3d electrons in molecule Xe@C₆₀: Interplay of intradoublet and confinement resonances. *Physical Review A* **2007**, *75*, 043201 1-6.
- [102] Grum-Grzhimailo, A. N.; Lucchese, R. R.; Prümper, G.; Ueda, K. A symmetry analysis of circular dichroism in photoabsorption of fixed-in-space molecules: Chiral and nondipole effects. *Journal of Electron Spectroscopy and Related Phenomena* **2007**, *155*, 104-108.
- [103] Kato, M.; Morishita, Y.; Oura, M.; Yamaoka, H.; Tamenori, Y.; Okada, K.; Matsudo, T.; Gejo, T.; Suzuki, I. H.; Saito, N. Absolute photoionization cross sections with ultra-high energy resolution for Ar, Kr, Xe and N₂ in inner-shell ionization regions. *Journal of Electron Spectroscopy and Related Phenomena* **2007**, *160*, 39-48.
- [104] Kumar, S. S.; Banerjee, T.; Deshmukh, P. C.; Manson, S. T. Spin-orbit-interaction activated interchannel coupling in dipole and quadrupole photoionization. *Physical Review A* **2009**, *79*, 043401 1-8.
- [105] Drube, W.; Grehk, T.M.; Thieß, S.; Pradhan, G. B.; Varma, H. R.; Deshmukh, P. C.; Manson, S. T. Pronounced effects of interchannel coupling in high-energy photoionization. *Journal of Physics B: Atomic, Molecular and Optical Physics* **2013**, *46*, 245006 1-6.
- [106] Southworth, S. H.; Wehlitz, R.; Picón, A.; Lehmann, C. S.; Cheng, L.; Stanton, J. F. Inner-shell photoionization and core-hole decay of Xe and XeF₂. *The Journal of Chemical Physics* **2015**, *142*, 224302 1-17.

- [107] Lawrence Berkeley National Lab. Center for X-ray Optics. X-ray data booklet. <http://xdb.lbl.gov/> (Accessed March 25, 2016).
- [108] Nakamura, M.; Sasanuma, M.; Sato, S.; Watanabe, M.; Yamashita, H.; Iguchi, Y.; Ejiri, A.; Nakai, S.; Yamaguchi, S.; Sagawa, T.; Oshio, T. Absorption Structure Near the K Edge of the Nitrogen Molecule. *Physical Review* **1969**, *178*, 80-82.
- [109] Dehmer, J. L.; Dill, D. Shape Resonances in K-Shell Photoionization of Diatomic Molecules. *Physical Review Letters* **1975**, *35*, 213-215.
- [110] Rescigno, T. N.; Langhoff, P. W. K-Shell Photoionization in Molecular Nitrogen. *Chemical Physics Letters* **1977**, *51*, 65-70.
- [111] Bianconi, A.; Petersen, H.; Brown, F. C.; Bachrach, R. Z. K-shell photoabsorption spectra of N₂ and N₂O using synchrotron radiation. *Physical Review A* **1978**, *17*, 1907-1911.
- [112] Dehmer, J. L.; Dill, D.; Wallace, S. Shape-Resonance-Enhanced Nuclear-Motion Effects in Molecular Photoionization. *Physical Review Letters* **1979**, *43*, 1005-1008.
- [113] Rescigno, T. N.; Gerwer, A.; McKoy, B. V.; Langhoff, P. W. On π -Shell Photoionization in Molecular Nitrogen. *Chemical Physics Letters* **1979**, *66*, 116-120.
- [114] Lindle, D. W.; Truesdale, C. M.; Kobrin, P. H.; Ferrett, T. A.; Heimann, P. A.; Becker, U.; Kerkhoff, H. G.; Shirley, D. A. Nitrogen K-shell photoemission and Auger emission from N₂ and NO. *The Journal of Chemical Physics* **1984**, *81*, 5375-5378.
- [115] Lynch, D. L.; McKoy, V. Relaxation effects in molecular K-shell photoionization. *Physical Review A* **1984**, *30*, 1561-1564.
- [116] Sodhi, R. N. S.; Brion, C. E. Reference Energies for Inner-Shell Electron Energy-Loss Spectroscopy. *Journal of Electron Spectroscopy and Related Phenomena* **1984**, *34*, 363-372.
- [117] Senn, P.; Grimm, F. A. Effects of dynamic symmetry breaking on cross-sections and angular distributions in the photoionization of molecular nitrogen. *Journal of Molecular Structure (Theochem)* **1995**, *342*, 109-114.
- [118] Shigemasa, E.; Adachi, J.; Oura, M.; Yagishita, A. Angular Distributions of 1s σ Photoelectrons from Fixed-in-Space N₂ Molecules. *Physical Review Letters* **1995**, *74*, 359-362.

- [119] Kempgens, B.; Kivimäki, A.; Neeb, M.; Köppe, H. M.; Bradshaw, A. M.; Feldhaus, J. A high-resolution N 1s photoionization study of the N₂ molecule in the near-threshold region. *Journal of Physics B: Atomic, Molecular and Optical Physics* **1996**, *29*, 5389-5402.
- [120] Samson, J. A. R.; Stolte, W. C.; He, Z. X.; Cutler, J. N.; Hansen, D. Postcollision interactions in the Auger decay of the Ar L shell. *Physical Review A* **1996**, *54*, 2099-2106.
- [121] Ito, K. New insights on the shape resonances in the K-shell continua of the N₂ and CO prototype molecules. *Journal of Electron Spectroscopy and Related Phenomena* **2001**, *114-116*, 15-22.
- [122] Weber, T.; Jagutzki, O.; Hattass, M.; Staudte, A.; Nauert, A.; Schmidt, L.; Prior, M. H.; Landers, A. L.; Bräuning-Demian, A.; Bräuning, H.; Cocke, C. L.; Osipov, T.; Ali, I.; Muiño, R. D.; Rolles, D.; Abajo, F J García de; Fadley, C. S.; Hove, M. A. V.; Cassimi, A.; Schmidt-Böcking, H.; Dörner, R. K-shell photoionization of CO and N₂: is there a link between the photoelectron angular distribution and the molecular decay dynamics? *Journal of Physics B: Atomic, Molecular and Optical Physics* **2001**, *34*, 3669-3678.
- [123] Ehara, M.; Makochekanwa, C.; Ueda, K.; Matsumoto, M.; Tanaka, T.; Prümper, G.; Harries, J.; Hatamoto, T.; Liu, X.; Lischke, T.; Tanaka, H.; Hoshino, M.; Tamenori, Y.; Nakatsuji, H. Symmetry-dependent vibrational excitation in N 1 s photoionization of N₂: Experiment and theory. *Journal of Chemical Physics* **2006**, *124*, 124311 1-8.
- [124] Hosaka, K.; Adachi, J.; Golovin, A. V.; Takahashi, M.; Teramoto, T.; Watanabe, N.; Yagishita, A.; Semenov, S. K.; Cherepkov, N. A. Non-dipole effects in the angular distribution of photoelectrons from the K-shell of N₂ molecule. *Journal of Physics B: Atomic, Molecular and Optical Physics* **2006**, *39*, L25-L34.
- [125] Yagishita, A.; Doerner, R.; Prior, M. H.; Hosaka, K. T.; Jagutzki, O.; Schmidt, L.; Landers, A. L.; Semenov, S. K.; Watanabe, N.; Schoeffler, M.; Weber, T.; Cherepkov, N. A.; Osipov, T.; Golovin, A. V.; Jahnke, T.; Schmidt-Boecking, H.; Takahashi, M.; Adachi, J. Nondipole effects in the angular distribution of photoelectrons from the C K shell of the CO molecule. *Physical Review. A* **2006**, *73*, 022716 1-8.
- [126] Rolles, D.; Braune, M.; Cvejanovic, S.; Gesner, O.; Hentges, R.; Korica, S.; Langer, B.; Lischke, T.; Prumper, G.; Reinkoster, A. Probing the transition from non-localization to localization by K-shell photoemission from isotope-substituted N₂. *Radiation Physics and Chemistry* **2006**, *75*, 1514-1518.
- [127] Semenov, S. K.; Cherepkov, N. A.; Matsumoto, M.; Hatamoto, T.; Liu, X.; Prümper, G.; Tanaka, T.; Hoashino, M.; Tanaka, H.; Gel'mukhanov, F.; Ueda, K. Interference modulation in the vibrationally resolved photoionization of the 1σ_g and 1σ_u core levels

of the N₂ molecule. *Journal of Physics B: Atomic, Molecular and Optical Physics* **2006**, *39*, L261-L267.

- [128] Stener, M.; Fronzoni, G.; Decleva, P.; Di Tommaso, D.; Powis, I. Theoretical study on the circular dichroism in core and valence photoelectron angular distributions of camphor enantiomers. *Journal of Chemical Physics* **2006**, *124*, 024326 1-10.
- [129] Toffoli, D.; Decleva, P. Photoelectron angular distributions beyond the dipole approximation: a computational study on the N₂ molecule. *Journal of Physics B: Atomic, Molecular and Optical Physics* **2006**, *39*, 2681-2691.
- [130] Cherepkov, N. A.; Semenov, S. K. New developments in the theory of molecular K-shell photoionization. *International Journal of Quantum Chemistry* **2007**, *107*, 2889-2901.
- [131] Bolognesi, P.; Toffoli, D.; Decleva, P.; Feyer, V.; Pravica, L.; Avaldi, L. The dipole and non-dipole parameters of the N K shell of the N₂ molecule up to 80 eV above threshold. *Journal of Physics B: Atomic, Molecular and Optical Physics* **2008**, *41*, 221002 1-5.
- [132] Schöffler, M.S.; Titze, J.; Petridis, N.; Jahnke, T.; Cole, K.; Schmidt, L. Ph. H.; Czasch, A.; Akoury, D.; Jagutzki, O.; Williams, J. B.; Cherepkov, N. A.; Semenov, S. K.; McCurdy, C. W.; Rescigno, T. N.; Cocke, C. L.; Osipov, T.; Lee, S.; Prior, M. H.; Belkacem, A.; Landers, A. L.; Schmidt-Böcking, H.; Weber, Th.; Dörner, R. Ultrafast Probing of Core Hole Localization in N₂. *Science* **2008**, *320*, 920-923.
- [133] Cahn, R.S.; Ingold, C.; Prelog, V. Specification of Molecular Chirality. *Angewandte Chemie* **1966**, *5*, 385-415.
- [134] Davies, P. T. On the Feynman rules for chiral interactions. *Journal of Physics A: Mathematical, Nuclear and General* **1973**, *6*, 1743.
- [135] Cherepkov, N. A. Manifestations of the optical activity of molecules in the dipole photoeffect. *Journal of Physics B: Atomic and Molecular Physics* **1983**, *16*, 1543-1548.
- [136] Engel, M.H.; Mack, S.A. Isotopic evidence for extraterrestrial non-racemic amino acids in the Murchison meteorite. *Nature* **1997**, *389*, 265-268.
- [137] Böwering, N.; Lischke, T.; Schmidtke, B.; Müller, N.; Khalil, T.; Heinzmann, U. Asymmetry in photoelectron emission from chiral molecules induced by circularly polarized light. *Physical Review Letters* **2001**, *86*, 1187-1190.

- [138] Rennie, E. E.; Powis, I.; Hergenbahn, U.; Kugeler, O.; Garcia, G.; Lischke, T.; Marburger, S. Valence and C 1s core level photoelectron spectra of camphor. *Journal of Electron Spectroscopy and Related Phenomena* **2002**, *125*, 197-203.
- [139] Garcia, G. A.; Nahon, L.; Lebech, M.; Houver, J.; Dowek, D.; Powis, I. Circular dichroism in the photoelectron angular distribution from randomly oriented enantiomers of camphor. *The Journal of Chemical Physics* **2003**, *119*, 8781-8784.
- [140] Hergenbahn, U.; Rennie, E. E.; Kugeler, O.; Marburger, S.; Lischke, T.; Powis, I.; Garcia, G. Photoelectron circular dichroism in core level ionization of randomly oriented pure enantiomers of the chiral molecule camphor. *The Journal of chemical physics* **2004**, *120*, 4553-4556.
- [141] Lischke, T.; Böwering, N.; Schmidtke, B.; Müller, N.; Khalil, T.; Heinzmann, U. Circular dichroism in valence photoelectron spectroscopy of free unoriented chiral molecules: Camphor and bromocamphor. *Physical Review A* **2004**, *70*, 022507 1-12.
- [142] Allegretti, F.; Polcik, M.; Sayago, D. I.; Demirors, F.; O'Brien, S.; Nisbet, G.; Lamont, C. L. A.; Woodruff, D. P. Can circular dichroism in core-level photoemission provide a spectral fingerprint of adsorbed chiral molecules? *New Journal of Physics* **2005**, *7*, 109 1-19.
- [143] Di Tommaso, D.; Stener, M.; Fronzoni, G.; Decleva, P. Conformational effects on circular dichroism in the photoelectron angular distribution. *Chemphyschem : a European journal of chemical physics and physical chemistry* **2006**, *7*, 924-934.
- [144] Harding, C. J.; Powis, I. Sensitivity of photoelectron circular dichroism to structure and electron dynamics in the photoionization of carvone and related chiral monocyclic terpenone enantiomers. *The Journal of Chemical Physics* **2006**, *125*, 234306 1-9.
- [145] Nahon, L.; Garcia, G. A.; Harding, C. J.; Mikajlo, E.; Powis, I. Determination of chiral asymmetries in the valence photoionization of camphor enantiomers by photoelectron imaging using tunable circularly polarized light. *The Journal of chemical physics* **2006**, *125*, 114309 1-14.
- [146] Dowek, D.; Lebech, M.; Houver, J. C.; Lucchese, R. R. Circular dichroism in molecular frame photoemission. *Molecular Physics* **2007**, *105*, 1757-1768.
- [147] Stener, M.; Toffoli, D.; Fronzoni, G.; Decleva, P. Recent advances in molecular photoionization by density functional theory based approaches. *Theor Chem Account* **2007**, *117*, 943-956.

- [148] Powis, I.; Harding, C. J.; Garcia, G. A.; Nahon, L. A valence photoelectron imaging investigation of chiral asymmetry in the photoionization of fenchone and camphor. *Chemphyschem : a European journal of chemical physics and physical chemistry* **2008**, *9*, 475-483.
- [149] Ulrich, V.; Barth, S.; Joshi, S.; Hergenhausen, U.; Mikajlo, E.; Harding, C. J.; Powis, I. Giant chiral asymmetry in the C 1s core level photoemission from randomly oriented fenchone enantiomers. *The Journal of Physical Chemistry A* **2008**, *112*, 3544-3549.
- [150] Turchini, S.; Catone, D.; Contini, G.; Zema, N.; Irrera, S.; Stener, M.; Di Tommaso, D.; Decleva, P.; Prosperi, T. Conformational effects in photoelectron circular dichroism of alaninol. *Chemphyschem : a European journal of chemical physics and physical chemistry* **2009**, *10*, 1839-1846.
- [151] Nahon, L.; Garcia, G. A.; Soldi-Lose, H.; Daly, S.; Powis, I. Effects of dimerization on the photoelectron angular distribution parameters from chiral camphor enantiomers obtained with circularly polarized vacuum-ultraviolet radiation. *Physical Review A* **2010**, *82*, 032514 1-10.
- [152] Lux, C.; Wollenhaupt, M.; Bolze, T.; Liang, Q.; Köhler, J.; Sarpe, C.; Baumert, T. Circular dichroism in the photoelectron angular distributions of camphor and fenchone from multiphoton ionization with femtosecond laser pulses. *Angewandte Chemie (International edition in English)* **2012**, *51*, 5001-5005.
- [153] Reid, K. L. Photoelectron angular distributions: developments in applications to isolated molecular systems. *Molecular Physics* **2012**, *110*, 131-147.
- [154] Garcia, G. A.; Nahon, L.; Daly, S.; Powis, I. Vibrationally induced inversion of photoelectron forward-backward asymmetry in chiral molecule photoionization by circularly polarized light. *Nature Communications* **2013**, *4*, 2132 1-5.
- [155] Castilho, R. B.; Ramalho, T. C.; Nunez, C. V.; Coutinho, L. H.; Santos, A. C. F.; Pilling, S.; Lago, A. F.; Silva-Moraes, M. O.; Souza, G. G. B. Single and double ionization of the camphor molecule excited around the C 1s edge. *Rapid Communications in Mass Spectrometry* **2014**, *28*, 1769-1776.
- [156] Garcia, G. A.; Dossmann, H.; Nahon, L.; Daly, S.; Powis, I. Photoelectron circular dichroism and spectroscopy of trifluoromethyl- and methyloxirane: a comparative study. *Physical Chemistry Chemical Physics* **2014**, *16*, 16214-16224.
- [157] Lestrangé, P. J.; Egidi, F.; Li, X. The consequences of improperly describing oscillator strengths beyond the electric dipole approximation. *The Journal of Chemical Physics* **2015**, *143*, 234103 1-8.

- [158] Lux, C.; Senftleben, A.; Sarpe, C.; Wollenhaupt, M.; Baumert, T. Photoelectron circular dichroism observed in the above-threshold ionization signal from chiral molecules with femtosecond laser pulses. *Journal of Physics B: Atomic, Molecular and Optical Physics* **2016**, *49*, 02LT01 1-7.
- [159] Ozga, C.; Jänkälä, K.; Schmidt, P.; Hans, A.; Reiß, P.; Ehresmann, A.; Kniw, A. X-ray absorption spectroscopy of the chiral molecules fenchone, α -pinene, limonene and carvone in the C 1s excitation region. *Journal of Electron Spectroscopy and Related Phenomena* **2016**, *207*, 34-37.

Curriculum Vitae

KYLE BOWEN

bowenk4@gmail.com

EDUCATION

University of Nevada Las Vegas, Las Vegas, NV

Ph.D. in Chemistry

2010-2016

University of Nevada Las Vegas, Las Vegas, NV

B.S. Chemistry

2009

AWARDS

Wolzing Family Research Scholarship

2015-2016

UNLV Department of Chemistry & Biochemistry Outstanding Graduate

Student Award

2015

Chateaubriand Fellowship

2013

Boyd Earl Award

2008 – 2009

NSF EPSCoR Summer UROP

2007

Frank and Mayme Stocker Scholarship

2006 – 2009

TEACHING EXPERIENCE

University of Nevada Las Vegas, Las Vegas, NV

Graduate Assistant-General Chemistry Lab

2011, 2014-2015

Graduate Assistant-Physical Chemistry Lab

2010

Graduate Assistant-Nursing Chemistry Lab

2010

RELATED EXPERIENCE

Université de Pierre et Marie Curie

**May - August 2012, October 2013 - August
2014**

Electron-ion coincidence experiments were performed as a result of a collaboration with the research group of Marc Simon, Ph.D. at Synchrotron SOLEIL near Paris, France.

PUBLICATIONS

- [1] **Bowen, K. P.**; Stolte, W. C.; Lago, A.F.; Dávalos, J. Z.; Piancastelli, M.N.; Lindle, D.W. Partial-ion-yield studies of SOCl_2 following x-ray absorption around the *S* and *Cl* K-edges. *Journal of Chemical Physics* **2012**, *137*, 204313.
- [2] McLaughlin, B.M., Balance, C.P.; **Bowen, K.P.**; Gardenghi, D.J.; Stolte, W.C. High Precision K-Shell Photoabsorption Cross Sections for Atomic Oxygen: Experiment and Theory. *The Astrophysical Journal Letters* **2013**, *77*, L8.
- [3] Guillemin, R.; Decleva, P.; Stener, M.; Bomme, C.; Marin, T.; Journal, L.; Marchenko, T.; Kushawaha, R. K.; Jänkälä, K.; Trcera, N.; **Bowen, K.P.**; Lindle, D.W.; Piancastelli, M.N.; Simon, M. Selecting core-hole localization or delocalization in CS_2 by photofragmentation dynamics. *Nature Communications* **2015**, *6*.

MEMBERSHIPS & POSITIONS

- University of Nevada Las Vegas Graduate and Professional Student Association (GPSA)
- Representative, Department of Chemistry and Biochemistry
- American Chemical Society
American Physical Society